S.T. Yau High School Science Award

Research Report

The Team

Name of team member: Xinyang Li
School: Oregon Episcopal School
City, Country: Oregon, USA

Name of supervising teacher: Thomas Lowery
Job Title: High School Teacher
School/Institution: Oregon Episcopal School
City, Country: Oregon, USA

Title of Research Report

Learning Compact Representations of Intrinsic-Alignment Responses for Weak Gravitational Lensing Cosmology

Date

2026/9/10

Learning Compact Representations of Intrinsic-Alignment Responses for Weak Gravitational Lensing Cosmology

Xinyang Li

Abstract

Weak gravitational lensing uses galaxy-shape correlations to study dark matter and cosmic expansion, but intrinsic alignments also contribute to these correlations. Allowing uncertain alignment responses to vary across scale and redshift can introduce many adjustable parameters. Can a compact representation preserve this flexibility without losing important features?

We construct a controlled family of positive alignment-response surfaces inspired by the nonlinear alignment (NLA) model, with 13 parameters governing redshift evolution and scale dependence. Numerical checks of random combinations and all parameter-domain corners precede the generation of 100,000 surfaces on a 31×101 grid. Using common training and validation samples, we compare principal component analysis (PCA), a convolutional autoencoder (Conv1D), and a PCA-assisted autoencoder at two to ten latent coordinates. Our investigation combines interpretable model design, matched-dimension reconstruction tests, and diagnostics of where compression fails.

The reported three-layer Conv1D model with six coordinates recovers 99.92% of the validation log-amplitude variance and has a mean relative amplitude error of 1.21%, a 41% reduction from six-component PCA. Ten Conv1D coordinates reduce the mean error to 0.23%. PCA-assisted compression achieves comparable averages with substantially fewer trainable parameters. However, the six-coordinate Conv1D model still reaches a 26.36% local error, showing that high variance recovery does not ensure uniform accuracy. Latent correlations reveal associations with model parameters but do not establish a unique physical interpretation.

These results demonstrate useful nonlinear compression within the sampled response family and identify the residual errors that further development must address. They are single-seed validation results; final test evaluation and propagation into lensing observables remain necessary. The method offers a concrete starting point for compact representations of alignment uncertainty in future weak-lensing analyses.

Keywords: cosmology; weak gravitational lensing; intrinsic alignment; dimensionality reduction; principal component analysis; autoencoder

Contents

1 Introduction **3**

2 Cosmological background and intrinsic alignment **4**
2.1 Cosmic expansion and the standard cosmological model 4
2.2 Observational constraints on dark energy 5
2.3 Weak gravitational lensing and matter clustering 6
2.4 Cosmic-shear surveys and the S_8 tension 8
2.5 Intrinsic alignment and galaxy-shape correlations 9
2.6 Intrinsic-alignment models and dimensionality reduction 11

3 Building the intrinsic-alignment model and dataset **13**
3.1 From three-dimensional IA power to the response amplitude 13
3.2 The broad redshift factor R_z 14
3.3 The luminosity factor R_L 14
3.4 The joint scale factor $S(k, z)$ 16
3.5 The combined shape amplitude and the IA power spectra 18
3.6 Sampling the response family and constructing the dataset 19

4 Dimensionality reduction with PCA and autoencoders **21**
4.1 Input representation and normalization 21
4.2 Linear and nonlinear compression 22
4.3 Convolutional autoencoder 22
4.4 PCA-assisted autoencoder 23
4.5 Training and model selection 24
4.6 Reconstruction metrics and interpretation 25

5 Results and discussion **26**
5.1 Model comparison and a compact working choice 26
5.2 PCA and the distribution of surface variation 28
5.3 Residual errors of the compact Conv1D model 29
5.4 Latent geometry and parameter associations 31
5.5 Limitations and the next methodological tests 33

6 Summary and conclusion **33**

Acknowledgements **35**

Declaration of AI use **35**

References **36**

1 Introduction

Weak gravitational lensing distorts the apparent shapes of distant galaxies, producing correlations that trace intervening matter. These correlations allow astronomers to study dark matter and test how structure grows as the Universe expands (Bartelmann & Schneider, 2001). Their interpretation, however, requires knowing which part of the measured signal comes from lensing.

Galaxies are not oriented independently of their surroundings. Their formation and evolution can produce correlated intrinsic shapes, known as *intrinsic alignments* (IA). These correlations enter the same measurements as lensing and can alter the inferred cosmological parameters if they are modelled inadequately (Chisari, 2025). This challenge becomes more demanding as surveys measure galaxy shapes with greater statistical precision.

A flexible IA model can accommodate changes with spatial scale, cosmic time, and galaxy population. Yet additional parameters can be difficult to constrain, and different combinations may produce similar predictions. This suggests a specific research question: how much of a flexible alignment response can be represented with fewer coordinates, and which features are lost as the representation becomes shorter? A successful compression would preserve the model's useful variation while providing a smaller space to explore. Whether it also improves a cosmological analysis is a separate question that requires testing against lensing observables.

We investigate the representation question using synthetic alignment-response surfaces. Each surface gives the response on a grid of wavenumber k, which labels spatial scale, and redshift z, which tracks cosmic expansion. We extend a nonlinear alignment (NLA) prescription with smooth factors controlling redshift and scale dependence (Bridle & King, 2007). Thirteen shape parameters define the family; the overall normalization and a prescribed cosmological factor remain separate. We check the numerical behaviour of the model across its parameter ranges and generate 100,000 surfaces, each containing 3,131 grid values rather than 3,131 independent physical parameters.

We compare three ways to encode each surface with a short vector of *latent coordinates*. Principal component analysis (PCA) reconstructs surfaces as linear combinations of shared patterns (Jolliffe & Cadima, 2016). A convolutional autoencoder learns nonlinear encoding and reconstruction directly on the grid, while a PCA-assisted autoencoder first projects the surface onto a fixed linear basis and then compresses its coefficients (Hinton & Salakhutdinov, 2006). The comparison uses the same 80,000 training and 10,000 validation surfaces at latent dimensions $L \in \{2, 4, 6, 8, 10\}$. Preprocessing is fitted on training data. We examine average reconstruction errors, difficult surfaces, and associations between the learned coordinates and the generating parameters. The remaining 10,000 samples are reserved for final test evaluation after model choices are fixed.

PCA and autoencoders are established methods, and neural networks already accelerate cosmological calculations (Spurio Mancini et al., 2022). The contribution here is their controlled application to a deliberately flexible IA response family: interpretable model construction is linked to a comparison at equal representation length and to diagnostics of the approximation's limits. Six Conv1D coordinates reach our reference target of 99.9% recovered validation variance, with substantially lower mean relative error than six-component PCA. The remaining local errors show why variance recovery alone is insufficient. This combination of a compact representation and explicit failure diagnostics provides a basis for further tests with observables.

Section 2 introduces the cosmological background and explains how intrinsic alignment enters galaxy-shape correlations. Section 3 defines the response model and its sampling. Section 4 describes the compression methods, training, and accuracy measures. Section 5 compares the results and examines their limitations, and Section 6 draws the methodological conclusions and sets out the steps towards survey use.

2 Cosmological background and intrinsic alignment

The motivation for modelling intrinsic alignment follows from the use of galaxy shapes to study cosmic expansion and the growth of structure. This section introduces the cosmological model and its observational tests, then develops the connection between weak gravitational lensing, intrinsic alignment, and the response-reconstruction problem investigated here.

2.1 Cosmic expansion and the standard cosmological model

Cosmology studies the Universe as a whole: its contents, history, and large-scale structure. The hot Big Bang model describes an early Universe that was much hotter and denser than it is today. As space expanded, the Universe cooled. Evidence for this history includes the *cosmic microwave background* (CMB), light that began travelling freely when the Universe was about 380,000 years old. The Planck satellite mapped its small temperature variations, which carry information about conditions in the early Universe (Planck Collaboration et al., 2020a). The hotter and colder regions in Figure 1 trace small differences in the early conditions from which cosmic structure grew. Their sizes and statistical distribution help constrain the Universe's contents and evolution.

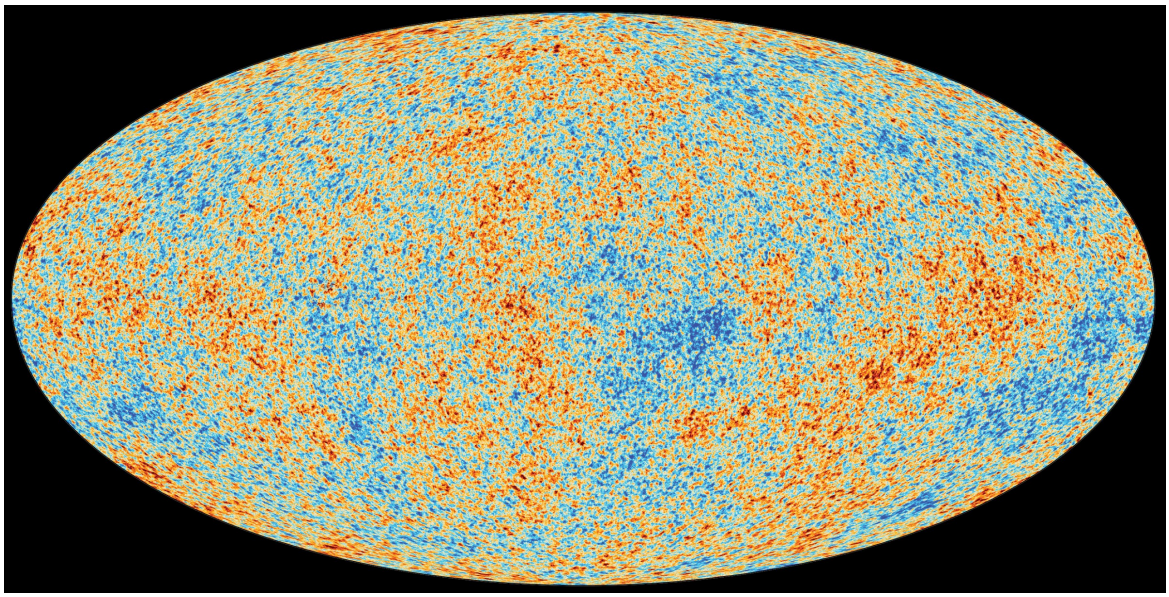


Figure 1: Planck's all-sky map of CMB temperature anisotropies. The colours show small temperature variations in light that began travelling freely about 380,000 years after the Big Bang. This is an early-Universe observation, rather than a map of present-day dark matter. Image credit: ESA/Planck Collaboration (Planck Collaboration et al., 2020a).

Expansion also stretches travelling light to longer wavelengths. We describe this *cosmological redshift* by

$$1 + z = \frac{\lambda_{\text{observed}}}{\lambda_{\text{emitted}}} = \frac{1}{a}, \tag{1}$$

where a is the scale factor, which tracks cosmic expansion and equals one today. Thus $z = 1$ means that the wavelength has doubled since emission. Larger cosmological redshifts generally let us study earlier times. They are not distances by themselves: converting redshift to distance requires an expansion model.

The standard cosmological model, called ΛCDM, includes a cosmological constant (Λ) and cold dark matter (CDM). It is also called the concordance model because it provides a common description of evidence from the CMB, galaxy distributions, and other observations. In this

model, about 5% of today's total energy density is ordinary matter, 27% is dark matter, and 68% is dark energy; these are approximate, model-dependent fractions (Planck Collaboration et al., 2020b). Ordinary matter includes atoms in stars and gas. The physical nature of the two dominant components, dark matter and dark energy, remains unresolved.

Dark matter contributes gravity but emits no light that we have detected. Galaxy motions and gravitational lensing reveal more gravitating matter than can be accounted for by visible stars and gas (Bartelmann & Schneider, 2001); the CMB also constrains its abundance (Planck Collaboration et al., 2020b). In ΛCDM, dark matter provides much of the gravitational attraction that builds galaxies and larger structures. "Cold" means that it moved slowly enough in the early Universe for small density fluctuations to grow. Its microscopic nature remains unknown.

Dark energy is the name given to the component used to explain the accelerated expansion first established with distant Type Ia supernovae (Riess et al., 1998). In general relativity, sufficiently negative pressure can cause cosmic expansion to accelerate. The simplest explanation is Λ, a cosmological constant whose energy density stays constant as space expands. Its physical origin is unexplained, and observations must test whether dark energy is constant or evolves. Weak gravitational lensing helps investigate both dark components by measuring matter clustering and its evolution within an expanding Universe.

2.2 Observational constraints on dark energy

To test the expansion history, astronomers need ways to compare distances at different times. The Dark Energy Spectroscopic Instrument (DESI) (Abdul Karim et al., 2025) measures galaxy and quasar redshifts over a large volume. Its measurements reveal *baryon acoustic oscillations* (BAO): a preferred separation in the distribution of matter, left by sound waves in the early Universe. This provides a statistical ruler whose apparent size changes with distance.

The second DESI data release, DR2, gives precise BAO measurements. Two quantities used to express these constraints are $\Omega_{\rm m}$, the present matter density divided by the critical density for a spatially flat Universe, and $H_0 r_d$. Here H_0 is today's expansion rate and r_d is the comoving length of the BAO ruler, with the overall expansion factored out. BAO constrains $H_0 r_d$ more directly than H_0 alone. In the left panel of Figure 2, the smaller DR2 contours compared with DR1 show how the additional observations narrow the allowed combinations of these quantities.

Dark energy's *equation-of-state parameter*, w, is its pressure divided by its energy density. A cosmological constant has $w = -1$. A common test allows

$$w(a) = w_0 + w_a(1 - a), \tag{2}$$

where w_0 is the value today and w_a controls how it changes. The constant case is $(w_0, w_a) = (-1, 0)$, marked by the dashed-line intersection in the right panel of Figure 2. The contours show how different data combinations constrain departures from that point.

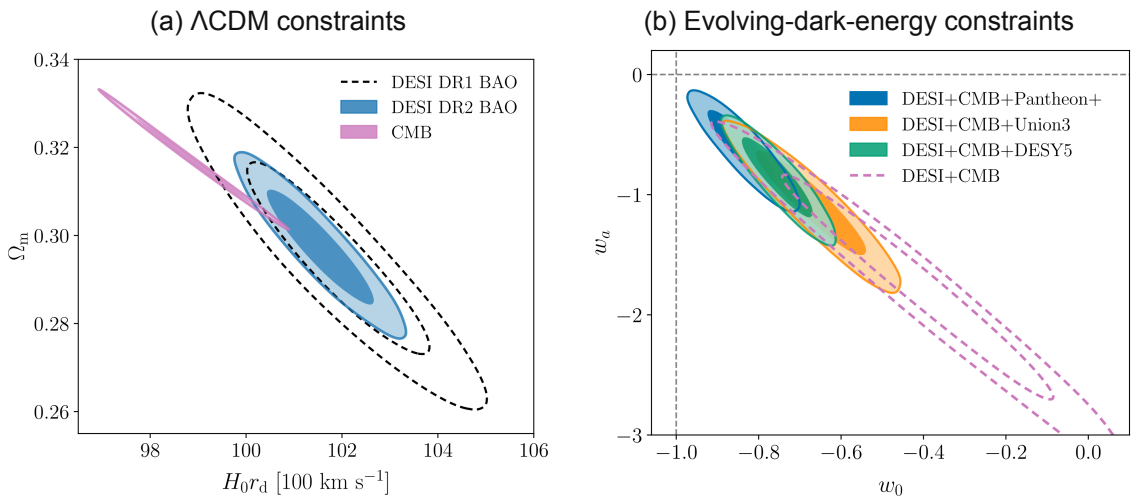


Figure 2: Two tests using DESI DR2 BAO measurements. Left: DR1, DR2, and CMB constraints on Ω_m and $H_0 r_d$ assuming ΛCDM; the horizontal axis expresses $H_0 r_d$ in units of $100\,\mathrm{km\,s^{-1}}$. Right: constraints on w_0 and w_a for the labelled data combinations. Contours enclose 68% and 95% of the posterior probability. The dashed-line intersection at $(-1, 0)$ marks a cosmological constant. Adapted from Abdul Karim et al. (2025), Figures 8 (left) and 11, under CC BY 4.0.

Type Ia supernovae provide another distance indicator: after correcting for differences between them, their brightnesses can be compared. In the DR2 BAO analysis, combining DESI with CMB measurements and different supernova samples gives a preference for evolution at about 2.8–4.2σ, depending on the combination (Abdul Karim et al., 2025). Here σ expresses statistical significance on a standard-deviation scale. This indication depends on the data and model assumptions, so it is not a confirmed discovery. A later DESI analysis (DESI Collaboration et al., 2026) adds information from absorption by intergalactic hydrogen. Its joint constraints also retain a preference for evolving dark energy, while showing that the strength of the evidence depends on the observations and modelling assumptions.

Confirmed evolution would challenge the cosmological-constant explanation of dark energy. Weak gravitational lensing provides a complementary test because its prediction depends on both the expansion history and the growth of matter fluctuations. This connection motivates the use of galaxy shapes as a cosmological observable.

2.3 Weak gravitational lensing and matter clustering

Gravity changes the paths of light rays. A large mass can produce obvious arcs or multiple images of a background galaxy, called strong gravitational lensing. In weak gravitational lensing, the changes are much smaller. *Convergence*, written κ, describes isotropic focusing: a small circular image changes size but stays circular. *Shear*, written γ, describes stretching in one direction and compression in the perpendicular direction. A circle then becomes an ellipse (Bartelmann & Schneider, 2001). Figure 3(a) shows where intervening matter deflects the light, while panel (b) separates the changes in apparent size and shape. In practice, these small distortions are inferred statistically from many galaxies.

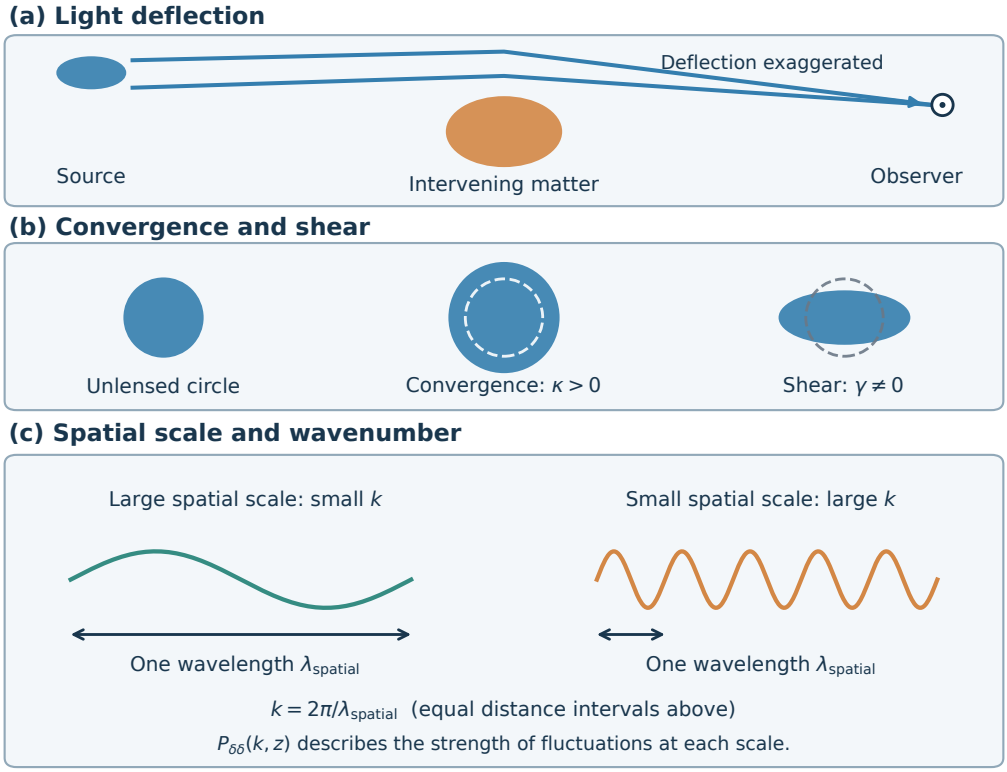


Figure 3: Weak gravitational lensing geometry, image distortions, and spatial scale. Intervening matter deflects light from distant galaxies. Convergence changes apparent size, while shear changes shape; distortions are exaggerated for clarity. Density waves over equal distance intervals illustrate the relation between spatial wavelength and wavenumber. These are schematic examples, not measured density fluctuations (Bartelmann & Schneider, 2001). Diagram prepared with AI assistance; source details are in the figure source record.

The matter distribution is inhomogeneous, with clusters, filaments, and underdense regions. We describe this *density field* by its density contrast,

$$\delta(\boldsymbol{x}, z) = \frac{\rho(\boldsymbol{x}, z) - \bar{\rho}(z)}{\bar{\rho}(z)}, \tag{3}$$

where ρ is the matter density at position $\boldsymbol{x}$ and $\bar{\rho}$ is its mean at that time. Positive δ denotes an overdense region. Instead of tracking every structure, we can describe the typical strength of fluctuations on different scales with the *matter power spectrum*, $P_{\delta\delta}(k, z)$. The wavenumber $k = 2\pi/\lambda_{\text{spatial}}$ labels a spatial wavelength: small k means large structures, and large k means small structures. Figure 3(c) illustrates this distinction using waves over equal distance intervals. This wavelength describes a density fluctuation, not the light used in Equation (1). We use comoving lengths, which factor out the overall expansion. A megaparsec (Mpc) is about 3.26 million light-years, so k can be expressed in Mpc^{-1}. The power spectrum describes the strength of density fluctuations as a function of scale and redshift. It carries the same two-point information as the correlation of density at pairs of positions, expressed in terms of spatial scales (Bartelmann & Schneider, 2001). It is therefore a useful statistical input for predicting cosmic shear.

On sufficiently large scales, small density fluctuations can be described by linear growth. On smaller scales, gravitational collapse couples their evolution and requires a nonlinear description. We denote the nonlinear matter power spectrum by $P_{\delta\delta}^{\text{NL}}(k, z)$. This is the matter-clustering input used by the IA response model in Section 3.

Astronomers estimate galaxy shapes, correct for image blurring and measurement bias, and estimate galaxy redshifts. They then measure how pairs of shapes are correlated at different

angular separations and in different redshift groups. This statistical weak gravitational lensing signal is called *cosmic shear*. Its prediction combines the matter power spectrum with the geometry between the observer, intervening matter, and source galaxies. This *line-of-sight projection* combines matter fluctuations over a broad range of distances and spatial scales, weighted by the lensing geometry. Weak gravitational lensing therefore tests both the growth of structure and the expansion history.

2.4 Cosmic-shear surveys and the S_8 tension

A useful quantity for comparing cosmic-shear measurements of matter clustering is

$$S_8 = \sigma_8 \sqrt{\Omega_\mathrm{m}/0.3}. \tag{4}$$

Here σ_8 measures the root-mean-square density contrast predicted today by linear growth theory, after averaging within spheres of radius $8h^{-1}\,\mathrm{Mpc}$, with $h = H_0/(100\,\mathrm{km\,s^{-1}\,Mpc^{-1}})$. Larger σ_8 means stronger matter fluctuations. Cosmic shear constrains the combination S_8 particularly well.

Three major Stage III imaging surveys are the Kilo-Degree Survey (KiDS) (Wright et al., 2025), the Dark Energy Survey (DES) (Amon et al., 2022), and the Hyper Suprime-Cam survey (HSC) (Li et al., 2023b). They use different combinations of area, depth, and image quality to constrain this quantity.

Some earlier shear analyses favoured a lower S_8 than the value predicted from the CMB within ΛCDM. This difference is known as the S_8 *tension*. The KiDS-1000 analysis (Asgari et al., 2021) found a difference of about 3σ; its later reanalysis (Li et al., 2023a) reduced this to about 2.3σ. KiDS-Legacy (Wright et al., 2025) is now consistent with Planck, with $S_8 = 0.815^{+0.016}_{-0.021}$. The shift mainly reflects improved redshift calibration, together with new survey area and improved image reduction.

HSC Year 3 (Li et al., 2023b) originally found $S_8 = 0.769^{+0.031}_{-0.034}$ from shape correlation functions. A reanalysis by Choppin de Janvry et al. (2025) uses DESI spectroscopy to calibrate the redshift distributions of these same source galaxies through their spatial clustering. It obtains $S_8 = 0.805 \pm 0.018$, closer to Planck and with smaller uncertainty. This is an improved analysis of the Year 3 shapes, rather than a new observing release. This shift illustrates why accurate galaxy redshifts matter for cosmology. Figure 4 shows the published comparison of KiDS-Legacy, DES Y3, and the original HSC Y3 analyses with Planck; it predates the HSC recalibration discussed here.

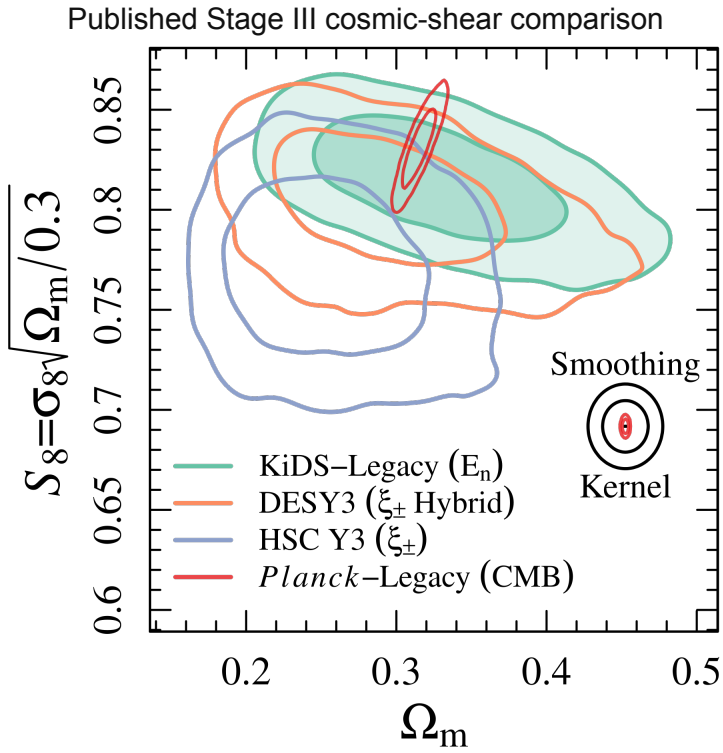


Figure 4: Published comparison of cosmic-shear constraints in the Ω_m–S_8 plane with Planck, adapted from Figure 14 of Wright et al. (2025), under CC BY 4.0. The legend identifies the analyses; the inset indicates the smoothing kernel. This comparison predates the HSC Y3 redshift-calibration update and DES Y6 results discussed in the text.

Another important uncertainty is *intrinsic alignment*: galaxy orientations can be correlated by their formation environments, adding to the correlations caused by lensing. This is the effect studied in this report. DES Year 6 (DES Collaboration et al., 2026) reports $S_8 = 0.798^{+0.014}_{-0.015}$ or $0.783^{+0.019}_{-0.015}$ for two different alignment models, discussed in Section 2.6. These are alternative analyses of the same observations, not two independent measurements. Here the difference arises from the alignment prescription, whereas the HSC shift above follows a change in redshift calibration. Recent results have reduced the S_8 tension in several analyses; the degree of agreement still depends on the data and modelling choices.

The next generation, often called Stage IV, includes Euclid (Euclid Collaboration et al., 2025), the Vera C. Rubin Observatory's Legacy Survey of Space and Time (Ivezić et al., 2019), and the Nancy Grace Roman Space Telescope (Eifler et al., 2021). These surveys combine wider sky coverage with deeper or sharper imaging. As statistical errors shrink, systematic effects become more important. These include shape and redshift calibration, the effect of gas and stars on matter clustering, and intrinsic alignment. Since alignment and matter clustering both contribute to shape correlations, uncertainty in the alignment response can propagate into the inferred clustering amplitude. This motivates a model that accommodates a range of alignment responses. The next subsection describes the physical origin of these correlations.

2.5 Intrinsic alignment and galaxy-shape correlations

Galaxies form and evolve within gravitational environments that can influence their shapes and orientations. The gravitational force varies across a galaxy and its surroundings; these spatial differences constitute a *tidal field*. Tidal forces can also exert torques that affect rotation. These mechanisms help explain why intrinsic alignments depend on galaxy population, environment, scale, and time. Observations and simulations support parts of this picture, but no single model

describes every population and scale equally well (Chisari, 2025). Changes in the observed population with redshift and differences in its environment across spatial scales motivate allowing both forms of dependence in the response model. These considerations guide the model's flexibility without determining a unique functional form.

A galaxy's *ellipticity* describes the elongation and orientation of its projected light distribution. Approximating its equal-brightness contours by ellipses with semimajor axis a, semiminor axis b, and position angle φ measured from a fixed sky axis, one common convention is

$$|e| = \frac{a-b}{a+b}, \qquad e_1 = |e|\cos(2\varphi), \qquad e_2 = |e|\sin(2\varphi). \tag{5}$$

A circular projected light distribution has $|e| = 0$, while a more elongated one has larger $|e|$. Here a, b denote galaxy semiaxes; the local use of a is separate from the cosmological scale factor in Equation (1). The factor of two accounts for the fact that rotating an ellipse by 180° leaves its shape unchanged. The two components describe both elongation and orientation. Other ellipticity conventions exist, so a shape estimator must be calibrated consistently with the definition it uses (Bartelmann & Schneider, 2001).

A telescope records a pixelated image blurred by the instrument and, for ground-based observations, the atmosphere. Even after correcting this blurring and measurement bias, an individual galaxy shape is a noisy estimate of shear because its intrinsic ellipticity is usually larger than the lensing distortion. To distinguish the contributions, we write the schematic weak-distortion relation

$$\underbrace{e^{\mathrm{O}}}_{\text{observed shape}} \simeq \underbrace{e^{\mathrm{I}}}_{\text{intrinsic shape}} + \underbrace{\gamma}_{\text{gravitational shear}} + \underbrace{n_e}_{\text{measurement noise}} . \tag{6}$$

Here O denotes observed and I denotes intrinsic; n_e represents the measurement error in ellipticity. Each term has two components. This schematic expression assumes that the estimator's response has been accounted for; it is not the exact transformation law of the geometrical ellipticity in Equation (5). The more precise lensing quantity is the reduced shear,

$$g = \frac{\gamma}{1-\kappa}, \tag{7}$$

which approaches γ when convergence is small (Bartelmann & Schneider, 2001).

Correlating shapes of distinct galaxies in redshift groups i, j produces several contributions. Measurement errors with zero mean that are uncorrelated between galaxies and with their physical shapes and shears do not contribute to the expected pair correlation. Expanding the intrinsic-shape and shear contributions gives, with angular and component labels suppressed,

$$\langle e_i^{\mathrm{O}} e_j^{\mathrm{O}} \rangle \simeq \mathrm{GG}_{ij} + \mathrm{GI}_{ij} + \mathrm{IG}_{ij} + \mathrm{II}_{ij}. \tag{8}$$

The brackets denote an average over distinct galaxy pairs, including when both galaxies belong to the same redshift group ($i = j$). Figure 5 separates the physical origins. In panel (a), correlated foreground matter shears both sources, producing GG. In panel (b), a shared tidal environment correlates intrinsic orientations, producing II; this is most relevant for physically close pairs. In panel (c), a foreground galaxy aligns with matter that also lenses a more distant source, producing an intrinsic–shear cross correlation even when the two galaxies are well separated. The orderings GI and IG identify which redshift group supplies each contribution. The two cross terms are often grouped as GI, giving the shorthand GG + GI + II. Observations constrain their sum; their different angular and redshift dependences help a model distinguish them. Random intrinsic shapes and uncorrelated measurement errors add variance, often called shape noise, whereas correlated measurement errors can bias the signal (Chisari, 2025).

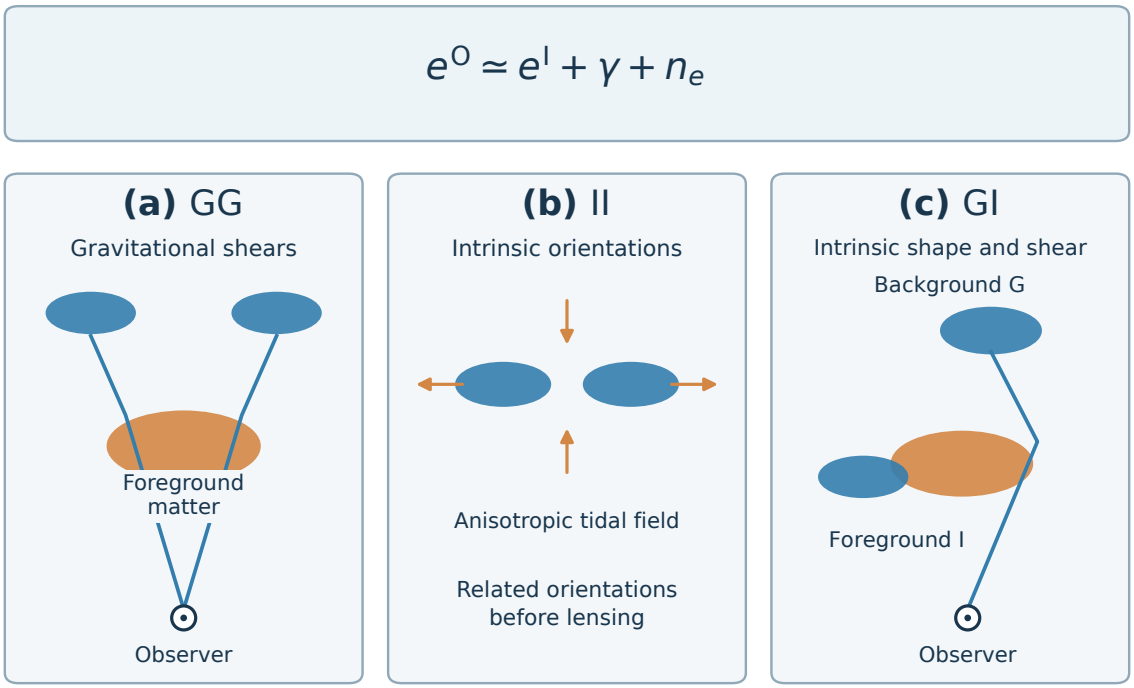


Figure 5: Contributions to observed galaxy-shape correlations. The relation between e^{O}, e^{I}, shear, and measurement noise n_e is schematic. (a) Lensing of two sources by correlated foreground matter. (b) Related galaxy orientations in a tidal environment. (c) A foreground intrinsic orientation correlated with background shear. Blue ellipses represent galaxies and orange marks intervening matter or tidal forces. Panel sizes do not indicate relative signal strengths (Chisari, 2025). Diagram prepared with AI assistance; source details are in the figure source record.

2.6 Intrinsic-alignment models and dimensionality reduction

The *linear alignment* (LA) model treats intrinsic shape as a leading-order response to the large-scale tidal field. The widely used *nonlinear alignment* (NLA) prescription retains this response structure but uses a nonlinear matter power spectrum to predict the correlations. Typical survey implementations describe the amplitude and redshift evolution with a few nuisance parameters: adjustable quantities that describe the alignment contribution when inferring cosmology (Bridle & King, 2007). NLA provides a compact prescription whose accuracy depends on the population and scales being analysed.

The *tidal alignment and tidal torquing* (TATT) model adds further responses, including terms quadratic in the tidal field and effects associated with how galaxies sample the density field (Blazek et al., 2019). It can describe more possibilities, usually with more adjustable parameters. Model suitability depends on the galaxy population, physical scales, statistical precision, and the assumed ranges and probabilities of the parameters, called *priors*.

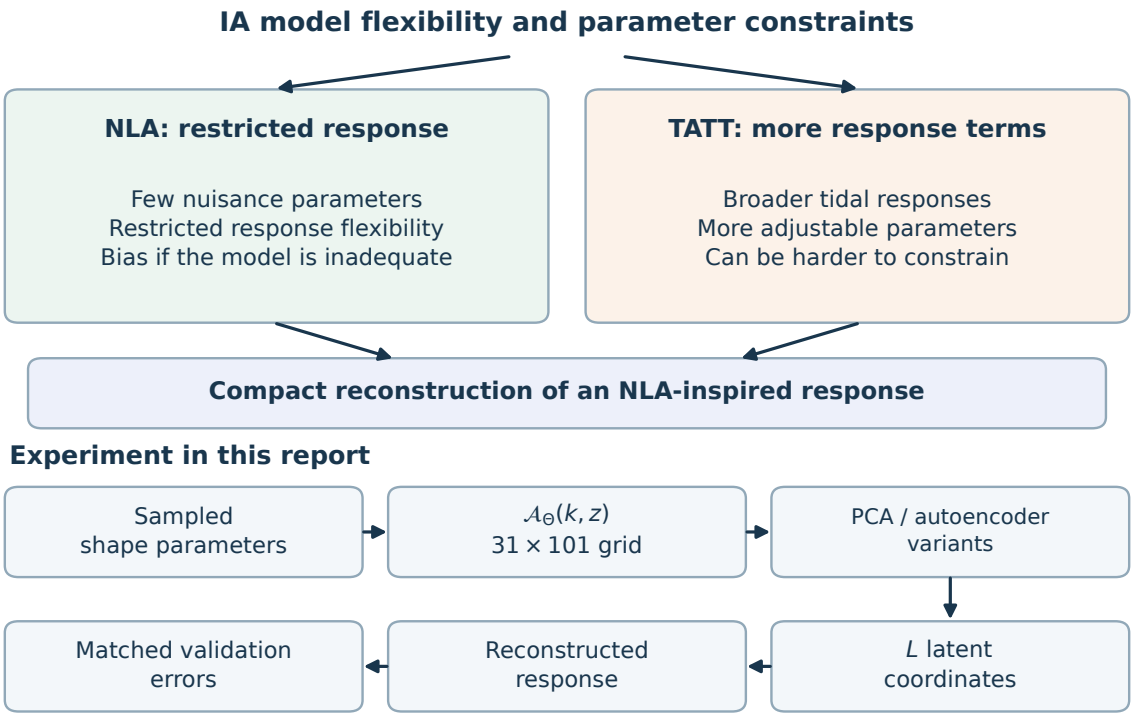


Figure 6: Model flexibility and compact response representations. Restricted models offer fewer parameters to constrain but allow fewer responses; flexible models can describe more responses while introducing poorly constrained directions. NLA and TATT provide the physical context (Bridle & King, 2007; Blazek et al., 2019). Our experiment tests reconstruction of an NLA-inspired response family at matched latent dimensions; it does not implement the full TATT model. Diagram prepared with AI assistance; source details are in the figure source record.

Model choice involves a balance between flexibility and the ability to constrain the parameters. An overly restricted model can attribute part of the alignment signal to a change in cosmology. A more flexible model can be harder to constrain and more costly to explore. For example, changing alignment strength can imitate part of a change in matter clustering. Such overlapping effects are called *parameter degeneracies*. Uncertainty in galaxy redshifts can introduce further overlap. The DES Year 6 comparison (DES Collaboration et al., 2026) illustrates that the alignment prescription can affect the inferred S_8.

Figure 6 connects this modelling challenge to our reconstruction experiment. Its upper boxes compare restricted and more flexible models; the lower workflow tests whether a flexible response can be represented using fewer coordinates. We construct an NLA-inspired model for a flexible IA response across scale and redshift. This response, $\mathcal{A}_\Theta(k, z)$, is a positive surface whose variation is specified by the shape parameters introduced in Section 3.

Different parameter combinations can produce similar response surfaces, and neighbouring points on each surface vary smoothly. These similarities motivate testing whether the main variation can be represented with fewer coordinates. The attainable reduction depends on the sampled family and the reconstruction accuracy required, so it must be assessed on held-out surfaces: examples not used to fit the representation.

Machine learning is already being applied to IA. IAEmu predicts galaxy clustering and alignment correlation functions from halo-based inputs (Pandya et al., 2025), while DELTA learns probabilistic galaxy orientations from local environments (Craigie et al., 2025). Our question concerns the compact reconstruction of a prescribed response family, rather than learning galaxy alignments directly from a catalogue.

We compare principal component analysis (PCA), a linear method, with nonlinear autoencoder variants at matched latent dimensions on the same validation samples. The *latent coordinates* form the compact numerical description from which a surface is reconstructed. The object being compressed is the flexible IA response. TATT provides physical context, but its additional terms are outside this response family. The present experiment measures reconstruction accuracy. Establishing whether the representation is useful for cosmological inference will also require testing its effect on lensing predictions and inferred parameters. Section 3 defines the response family and the dataset used to evaluate its reconstruction.

3 Building the intrinsic-alignment model and dataset

To evaluate compact representations, we require a controlled family of IA responses with known variation across scale and redshift. We retain the NLA relations between matter and alignment spectra, then introduce smooth factors that allow the response to vary within this prescription. Separating these factors makes their effects interpretable and provides a reproducible way to generate synthetic surfaces. The resulting flexible IA response model is phenomenological: we choose functions with specified behaviours to represent a range of possible responses. These choices define the reconstruction experiment; they do not constitute a complete theory of galaxy formation. We explain each factor through its defining equation and characteristic behaviour, combine the factors into a response surface, and then describe how the family is sampled.

3.1 From three-dimensional IA power to the response amplitude

The angular correlations in Section 2.5 are predicted from three-dimensional spectra. The matter–intrinsic spectrum $P_{\delta I}$ describes the correlation of matter density with intrinsic galaxy shape, while $P_{\rm II}$ describes intrinsic-shape correlations. In the adopted NLA-inspired prescription,

$$P_{\delta I}(k,z) = \mathcal{A}_{\rm IA}(k,z) P_{\delta\delta}^{\rm NL}(k,z), \qquad P_{\rm II}(k,z) = \mathcal{A}_{\rm IA}^2(k,z) P_{\delta\delta}^{\rm NL}(k,z). \tag{9}$$

Here $P_{\delta\delta}^{\rm NL}(k,z)$ is the nonlinear matter power spectrum. The comoving wavenumber k specifies spatial scale, with larger k corresponding to smaller scales, and z is redshift. The response enters once when one member of the correlation is an intrinsic shape, and twice when both are. A survey prediction projects these spectra along the line of sight, with the appropriate galaxy distributions and lensing geometry, to obtain the angular GI, IG and II contributions (Bridle & King, 2007).

We separate the signed IA amplitude into

$$\mathcal{A}_{\rm IA}(k,z) = -A_0\, \mathcal{A}_\Omega(z)\, \mathcal{A}_\Theta(k,z). \tag{10}$$

The constant A_0 sets the overall strength, and the cosmological factor is

$$\mathcal{A}_\Omega(z) = C_{\rm NLA} \frac{\Omega_{\rm m}}{D(z)}, \tag{11}$$

where $\Omega_{\rm m}$ is the present matter density divided by the present critical density, and $D(z)$ is the linear growth factor, normalized to $D(0) = 1$. The dimensionless normalization $C_{\rm NLA} = 0.0134$ includes the product usually written $C_1 \rho_{\rm crit}$, with $\rho_{\rm crit}$ the present critical density. The inverse-growth dependence is part of the adopted NLA prescription: as $D(z)$ decreases towards higher redshift, $\mathcal{A}_\Omega$ increases. This factor is computed from the background cosmology and is separate from the sampled shape parameters.

The positive response surface is

$$\mathcal{A}_\Theta(k,z) = R_z(z) R_L(z) S(k,z) > 0. \tag{12}$$

The factor R_z allows a broad redshift trend, R_L represents an additional trend motivated by luminosity and population changes, and S describes scale dependence. Their product supplies the family of surfaces used to compare PCA and autoencoder reconstruction.

We compress $\log_{10} \mathcal{A}_\Theta$. This separates reconstruction of the flexible response from the external normalization A_0 and the prescribed cosmological factor. Amplitude variation across the surface is still retained. Section 4 defines the input transformation and normalization.

3.2 The broad redshift factor R_z

The inverse-growth factor alone need not describe how the alignment of an observed galaxy population evolves. We allow residual evolution relative to a fixed pivot $z_* = 0.5$ by defining

$$r(z) = \frac{1+z}{1+z_*}, \qquad R_z(z) = r^\eta(z). \tag{13}$$

The ratio r is dimensionless and equals one at the pivot, so $R_z(z_*) = 1$ for every η. The pivot therefore supplies a common normalization rather than a preferred transition in the evolution.

Figure 7 illustrates the effect of η. Positive values give a larger response above the pivot and a smaller one below it; negative values reverse this trend. At $\eta = 0$, $R_z = 1$. Because R_z depends only on redshift, it rescales the response uniformly across wavenumber at each fixed z.

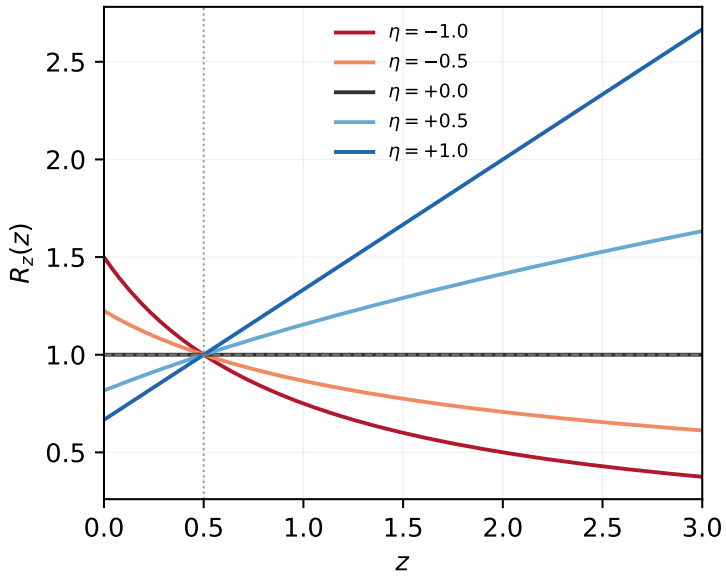


Figure 7: Broad redshift factor $R_z(z)$ for $\eta \in \{-1, -0.5, 0, +0.5, +1\}$. The dotted vertical line marks $z_* = 0.5$ and the dashed horizontal line marks $R_z = 1$. Redder curves have more negative η, bluer curves have more positive η, and the black curve has $\eta = 0$. All curves are normalized to unity at the pivot.

3.3 The luminosity factor R_L

A survey's luminosity distribution and population mix can evolve with redshift, changing the alignment response of the observed galaxies. Multiplying R_z by a second power law would only change its overall exponent. We instead introduce a smooth transition, allowing a change in the rate of evolution that a single power law cannot describe. The luminosity factor $R_L(z)$ represents this additional population-dependent trend and shares the normalization pivot of R_z. We do not fit a survey luminosity function here.

Three parameters describe this factor: z_q locates the transition, ξ controls the direction and strength of the additional evolution, and $s > 0$ controls the transition sharpness. With $r_q = (1 + z_q)/(1 + z_*)$, we choose

$$R_L(z) = \left[\frac{1 + [r(z)/r_q]^s}{1 + (1/r_q)^s}\right]^{\xi/s}. \tag{14}$$

The numerator changes smoothly as $r/r_q = (1 + z)/(1 + z_q)$ passes through unity. At $z = z_*$, the numerator equals the denominator, giving $R_L(z_*) = 1$. This normalization separates evolution relative to the pivot from the overall amplitude.

Figure 8 illustrates these three controls in the order z_q, ξ and s.

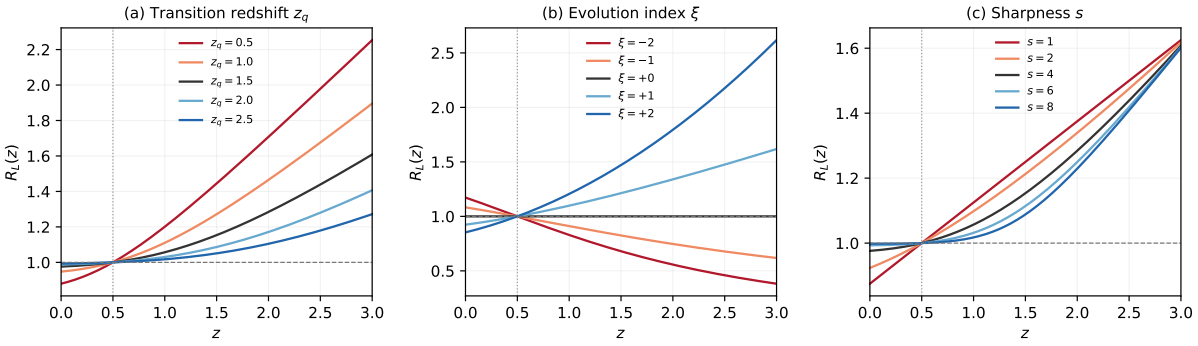


Figure 8: Luminosity factor $R_L(z)$ with one parameter varied in each panel. (a) Transition redshift $z_q \in \{0.5, 1.0, 1.5, 2.0, 2.5\}$ at $\xi = 1$ and $s = 4$. (b) Evolution index $\xi \in \{-2, -1, 0, +1, +2\}$ at $s = 2$ and $z_q = 1.5$. (c) Sharpness $s \in \{1, 2, 4, 6, 8\}$ at $\xi = 1$ and $z_q = 1.5$. The pivot and unit guides have the same meaning as in Figure 7. The larger sharpness in panel (a) makes the transition more visible. The illustrative $\xi = \pm 2$ curves extend beyond the dataset's sampling interval; the black curve in panel (b) has $\xi = 0$ and hence $R_L = 1$.

In panel (a), increasing z_q moves the transition to higher redshift, corresponding to earlier cosmic time. Since every curve passes through $R_L = 1$ at $z_* = 0.5$, moving the transition also changes the response relative to that fixed reference.

In panel (b), positive ξ increases R_L above the pivot, negative ξ decreases it, and $\xi = 0$ gives unity at every redshift. In this last case there is no luminosity transition, and z_q and s have no effect on the response.

In panel (c), smaller s spreads the transition over a broader redshift interval, while larger s concentrates it around z_q. Far above the transition, R_L approaches a power law in $1 + z$ with exponent ξ. Changing s can also change the normalization of that trend, even though its limiting exponent stays the same. The plotted interval need not reach this limit; its visible curvature is the additional freedom supplied by R_L.

The distinction between these controls can also be seen from the local logarithmic slope,

$$\frac{d\ln(R_z R_L)}{d\ln(1+z)} = \eta + \xi \frac{[(1+z)/(1+z_q)]^s}{1 + [(1+z)/(1+z_q)]^s}. \tag{15}$$

The broad contribution is η, while the additional contribution changes smoothly towards ξ and equals $\xi/2$ at $z = z_q$. Consequently, η and ξ can partly compensate over a limited redshift interval. The plots illustrate distinct controls, but do not imply that observations could determine all of them independently.

3.4 The joint scale factor $S(k, z)$

The redshift-only factors change the response uniformly across spatial scales. They cannot describe a small-scale alignment response that differs from its large-scale behaviour. We therefore introduce a smooth correction $S(k, z)$ that approaches unity on large scales and can vary at higher wavenumber. It modifies the IA response; the nonlinear evolution of the matter spectrum is already included in $P_{\delta\delta}^{\rm NL}(k, z)$.

The scale response has a transition wavenumber k_t, an onset sharpness n, a high-wavenumber correction index α, and a tail-curvature parameter m. We allow these quantities to evolve smoothly through the same redshift ratio $r(z)$:

$$\begin{aligned} k_t(z) &= k_{t,*}\, r^{\gamma_t}(z), \quad & n(z) &= n_*\, r^{\gamma_n}(z), \\ \alpha(z) &= \alpha\, r^{\gamma_\alpha}(z), \quad & m(z) &= m\, r^{\gamma_m}(z). \end{aligned} \tag{16}$$

The constants $k_{t,*}$, n_*, α and m are the values at z_*. Each γ controls evolution away from that pivot; setting it to zero makes the corresponding quantity constant. This evolution keeps k_t, n and m positive and preserves the sign of α for the adopted parameter ranges.

Using the dimensionless ratio $x = k/k_t(z)$, we define

$$S(k, z) = 1 + q\, \frac{x^{n(z)}}{1 + x^{n(z)}} \left(\frac{1 + x^{m(z)}}{2} \right)^{\alpha(z)/m(z)} . \tag{17}$$

The first factor in the correction, $x^n/(1 + x^n)$, rises smoothly from zero to one and controls its onset. The second factor adjusts the high-wavenumber behaviour, while q sets the strength of the correction.

Three simple properties clarify the construction:

$$\begin{aligned} S(k, z) &\longrightarrow 1 \quad \text{as } k \longrightarrow 0 \text{ at fixed } z, \\ q = 0 \implies S(k, z) &= 1, \qquad S(k_t(z), z) = 1 + \frac{q}{2}. \end{aligned} \tag{18}$$

The first recovers the large-scale baseline, and the second removes all scale dependence. For the transition value, substituting $k = k_t(z)$ gives $x = 1$: the onset factor is $1/2$ and the tail factor is one. This explains the division by two in Equation (17). At fixed redshift, for $q > 0$ and $k \gg k_t(z)$, the correction follows $S - 1 \propto [k/k_t(z)]^{\alpha(z)}$. The exponent therefore describes the high-k correction, rather than the full factor including its unit baseline.

Figure 9 shows a fiducial example with positive α. The large-scale region remains close to $S = 1$, while the correction increases towards smaller scales. Evolution of the scale parameters allows the position and shape of this pattern to vary with redshift.

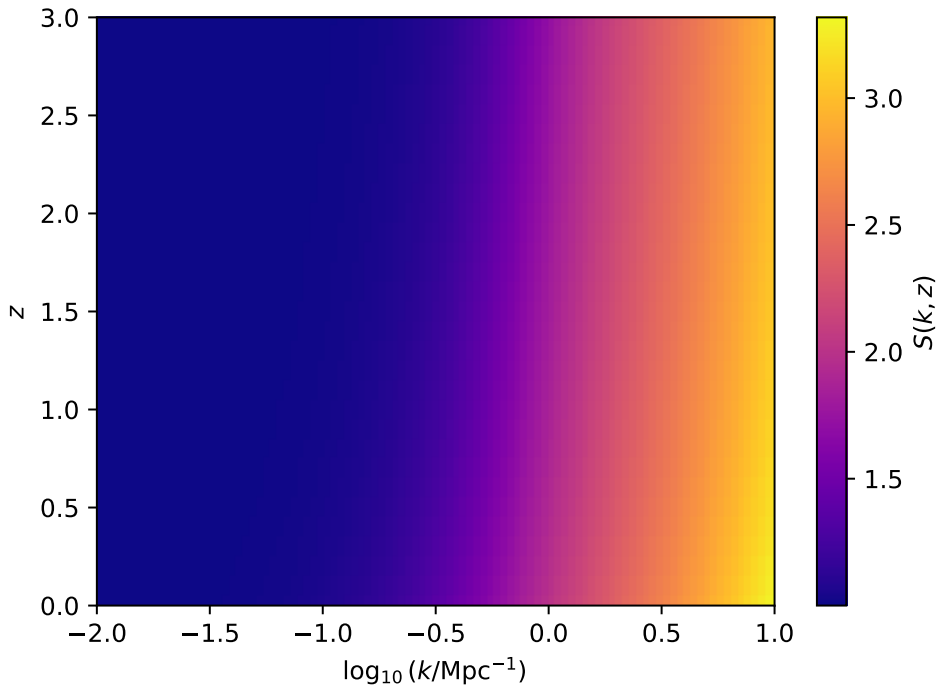


Figure 9: Fiducial scale–redshift factor $S(k, z)$ on the model grid. The horizontal axis is $\log_{10}(k/\mathrm{Mpc}^{-1})$, so the left side of the panel shows large-scale modes and the right side shows small-scale modes. The vertical axis is redshift from $z = 0$ to $z = 3$. Colour is the value of S itself. At $z_* = 0.5$ the fiducial choices are $k_{t,*} = 0.5\,\mathrm{Mpc}^{-1}$, $q = 1$, $n_* = 2$, $\alpha = 0.3$, and $m = 2$. Their evolution uses $\gamma_t = 0.4$, $\gamma_n = 0.2$ and $\gamma_\alpha = \gamma_m = 0$. The response approaches unity at low k and increases at high k for this fiducial choice.

The five scale controls have the following roles:

Correction strength, q. This parameter multiplies the scale-dependent contribution, with Equation (18) relating it to the response at the transition. When the correction is absent, the remaining scale parameters have no effect.

Transition scale, $k_t(z)$. The ratio k/k_t locates the transition from the large-scale baseline. Increasing k_t moves the transition to smaller comoving scales. Positive γ_t places it at higher wavenumber above the pivot. This is a model transition, not a measured boundary between physical regimes.

Transition sharpness, $n(z)$. Smaller n makes the onset factor change over a broader range of scales; larger n concentrates that change near k_t. The tail factor determines how the correction continues beyond this onset.

High-k behaviour, $\alpha(z)$. Positive values produce a growing high-k correction, while negative values make it decay towards zero at sufficiently high k, returning S towards unity. At $\alpha = 0$, the tail factor is one and $S \longrightarrow 1 + q$ as k increases.

Tail curvature, $m(z)$. This parameter controls how smoothly the tail factor approaches its high-k trend and can change the normalization of that trend. It complements n, which controls the onset factor. When $\alpha = 0$, both m and its evolution index have no effect.

The sampled range uses $q \geq 0$. Both factors multiplying q are positive, so $S \geq 1$: the scale correction enhances the response relative to the redshift-only baseline. A negative α reduces this enhancement at sufficiently high k but does not produce suppression below the baseline. This restriction defines the scope of the response family. The controls describe features of a surface rather than independently measured galaxy properties. Their effects can overlap or disappear in the limiting cases above, motivating a search for compact representations.

These limits also give testable reasons for unequal parameter sensitivity. When q is small, changing the other scale parameters has little effect on the full surface. When α is close to zero, the tail-curvature parameters are weakly expressed. Such overlaps can make approximate compression efficient without reducing the exact number of parameters that define the model family.

3.5 The combined shape amplitude and the IA power spectra

Multiplying R_z, R_L and S gives the response surface that is later compressed. All three factors are positive for the adopted parameter ranges, so $\mathcal{A}_\Theta > 0$ and its logarithm is defined throughout the grid. Section 4 explains this input transformation. The pivot normalization fixes $R_z(z_*) = R_L(z_*) = 1$, so the combined response there is $\mathcal{A}_\Theta(k, z_*) = S(k, z_*)$, which need not equal unity. The separate normalization A_0 and cosmological factor $\mathcal{A}_\Omega$ can then be applied to recover the signed amplitude in Equation (10).

Figure 10 shows the product of the three factors and connects their separate controls to variation across the full grid.

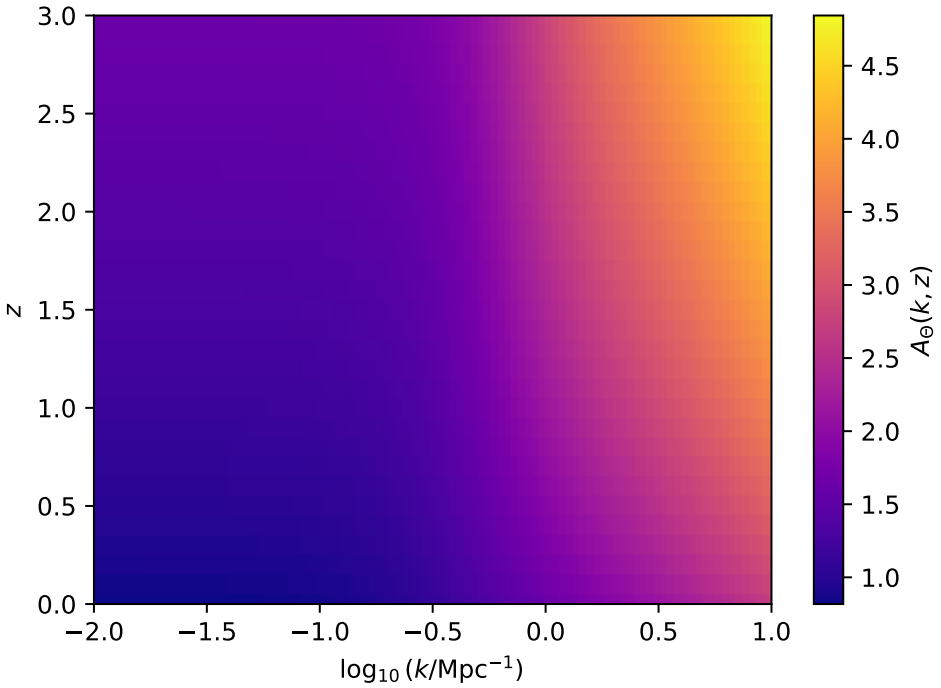


Figure 10: Fiducial shape amplitude $\mathcal{A}_\Theta(k, z) = R_z R_L S$ on the same (k, z) grid as Figure 9. The horizontal axis is $\log_{10}(k/\mathrm{Mpc}^{-1})$ and the vertical axis is redshift. Colour is the value of $\mathcal{A}_\Theta$. The fiducial luminosity parameters are $\xi = 0$, $s = 2$, and $z_q = 1$, so $R_L = 1$ and the extra redshift trend comes only from $\eta = 0.5$. Large-scale columns on the left are close to that redshift-only amplitude. Small-scale columns on the right are larger because the fiducial S exceeds unity.

At fixed redshift, this fiducial surface increases towards small scales because S increases with k. Its vertical variation combines R_z with the redshift evolution of the scale parameters. The choice $\xi = 0$ isolates these effects; the nontrivial luminosity trends are illustrated separately in Figure 8. Multiplication by $-A_0\mathcal{A}_\Omega(z)$ then gives the signed IA amplitude in Equation (10).

Figure 11 shows how this amplitude enters the three-dimensional spectra through Equation (9). The matter spectrum is determined independently of the IA response, while the two alignment spectra inherit its scale and redshift dependence.

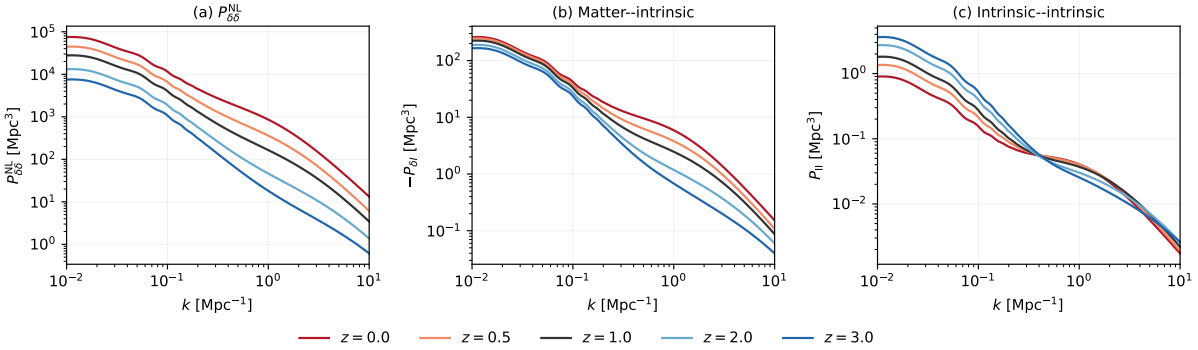


Figure 11: Three-dimensional spectra in the adopted NLA-inspired model: (a) nonlinear matter power $P_{\delta\delta}^{\rm NL}$, (b) the negative of the matter–intrinsic cross spectrum $-P_{\delta I}$, and (c) intrinsic auto-power $P_{\rm II}$. Both axes are logarithmic, with k in Mpc^{-1} and power in Mpc^3. Red to blue denotes $z = 0$, 0.5, 1, 2 and 3. The curves use the fiducial response of Figure 10 with $A_0 = 1$ and the notebook's Planck-like cosmology. Matter power is calculated with an Eisenstein–Hu transfer function and a Halofit nonlinear correction in PyCCL (Chisari et al., 2019). Panel (b) plots $-P_{\delta I}$ to show its magnitude on a logarithmic axis; the signed spectrum enters the model. These curves illustrate the prescription and are not fitted to survey measurements.

In panel (a), matter power is lower at higher redshift because structure has grown less. The curves generally decrease with increasing k over the plotted interval. Nonlinear enhancement refers to a comparison with linear matter power at the same scale; Figure 11 does not display that comparison.

Panel (b) scales matter power by one factor of $\mathcal{A}_{\rm IA}$. Where $S \simeq 1$, this is approximately a redshift-dependent rescaling. At smaller scales, the fiducial correction increases $|P_{\delta I}|/P_{\delta\delta}^{\rm NL}$.

Panel (c) contains two response factors, so this relative enhancement is stronger. The redshift ordering also changes between panels because the IA amplitude evolves as well as the matter spectrum. These are properties of the illustrated parameter choice; the sampled response family allows other trends.

3.6 Sampling the response family and constructing the dataset

We collect the shape parameters listed in Table 1 into the vector $\mathbf{\Theta}$, with $N_\Theta = 13$ entries. They control redshift and luminosity evolution, the scale response, and its redshift dependence. The external normalization A_0 and the cosmological factor $\mathcal{A}_\Omega$ are excluded from this vector and are not sampled. Sampling combinations of these controls provides known target surfaces for a comparison of compression methods, including responses that differ substantially from the fiducial example.

Table 1 defines the sampling distributions. These ranges specify the scope of the reconstruction experiment, providing varied responses while limiting exceptionally large variations within a surface. The transition wavenumber is sampled log-uniformly, assigning equal probability to equal multiplicative intervals; the other controls are sampled uniformly in their listed coordinates, independently of one another. We generate 100,000 surfaces on $N_z = 31$ equally spaced redshifts from $z = 0$ to $z = 3$ and $N_k = 101$ logarithmically spaced wavenumbers from $k = 0.01$ to $10\,\mathrm{Mpc}^{-1}$. Each surface is therefore an $N_z \times N_k$ array, with redshift along the first axis and wavenumber along the second.

Before fixing these bounds, we evaluated 8,192 random parameter combinations and all $2^{N_\Theta} = 8{,}192$ corners of the parameter domain. Every evaluated surface was finite and positive. The corner checks examine simultaneous extreme parameter choices that random sampling may miss. These checks also test whether the values remain within the computer's numerical range

Table 1: Sampling bounds for the synthetic IA response family. The ranges are design choices for this compression experiment, not observational constraints or posterior distributions from a galaxy survey. The bounds on $k_{t,*}$ are in Mpc^{-1}; all other parameters are dimensionless.

Parameter	Main effect	Range	Sampling
η	broad redshift trend	$[-1.5, 1.5]$	uniform
ξ	index of additional luminosity evolution	$[-1.5, 1.5]$	uniform
s	sharpness of the luminosity transition	$[1, 10]$	uniform
z_q	luminosity-transition redshift	$[0.5, 2.5]$	uniform
q	size of scale response	$[0, 2]$	uniform
n_*	scale-transition sharpness at the pivot	$[1, 5]$	uniform
$k_{t,*}$	pivot transition wavenumber	$[0.1, 1]$	log-uniform
α	high-k correction slope at the pivot	$[-0.4, 0.4]$	uniform
m	tail curvature at the pivot	$[1, 4]$	uniform
γ_t	redshift evolution of k_t	$[-0.5, 0.5]$	uniform
γ_n	redshift evolution of n	$[-0.35, 0.35]$	uniform
γ_α	redshift evolution of α	$[-0.25, 0.25]$	uniform
γ_m	redshift evolution of m	$[-0.2, 0.2]$	uniform

across the model grid; they do not establish observational validity or exhaust every combination within the parameter ranges.

We also checked that the chosen bounds retain varied surfaces without allowing a few extreme combinations to dominate their amplitude range. For a surface, define its internal range as the difference between the largest and smallest $\log_{10} \mathcal{A}_\Theta$ values, in dex. The 99th percentile of this range over the random checks is 1.656 dex, below the design ceiling of 1.75 dex; the largest corner range is 2.958 dex, below a 3.00 dex ceiling. The median, over grid points, of the random ensemble's 1st–99th percentile log-amplitude spread is 1.025 dex, above a 1.00 dex diversity reference. These are numerical design criteria for this experiment, not physical bounds derived from data.

Figure 12 shows the distribution of the random range-check surfaces. Their spread illustrates why reconstruction should be assessed across the family, including surfaces with large internal variation, rather than only near a single fiducial response.

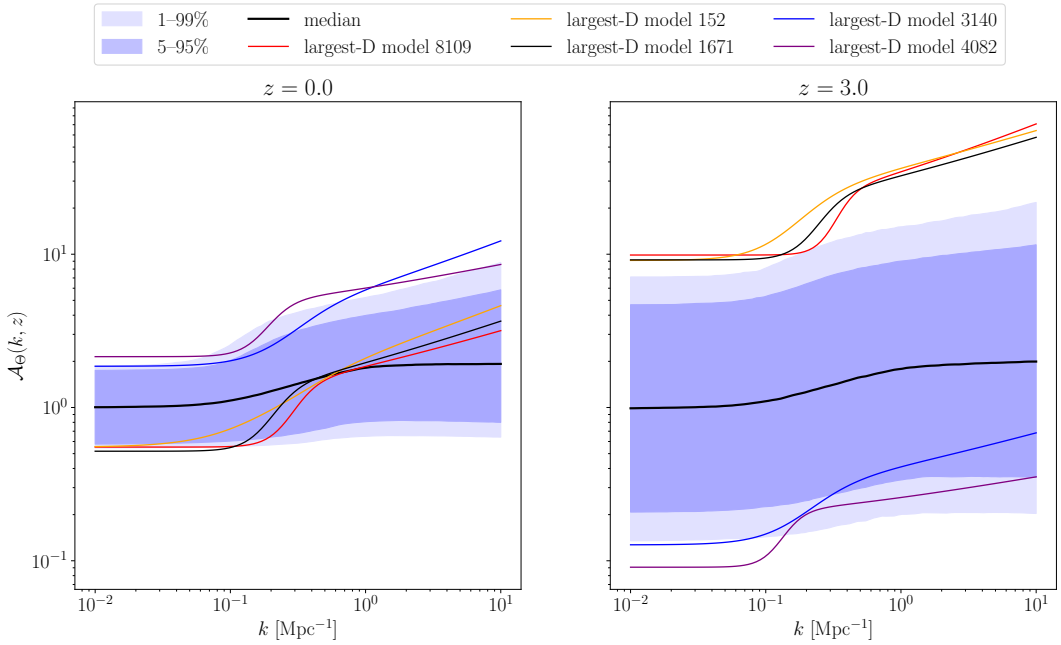


Figure 12: Distribution of 8,192 random sampling-range validation surfaces at $z = 0$ and $z = 3$. In each panel the horizontal axis is wavenumber k and the vertical axis is $\mathcal{A}_\Theta$. The shaded regions contain the central 98% and 90% of the surfaces at each k, the black curve is the median, and the coloured curves are the five surfaces with the largest internal dynamic range. This diagnostic ensemble is separate from the final 100,000-surface dataset.

The stored dataset is divided into 80,000 training surfaces, 10,000 validation surfaces and 10,000 test surfaces. Training determines the PCA basis, normalization statistics and network parameters. Validation is used to monitor training and compare architecture, latent-width and training choices. The test subset is reserved for the final performance evaluation after these choices are frozen. Fitting preprocessing steps only on the training subset prevents information from the held-out surfaces from entering those steps.

Each parameter vector determines all $N_z N_k$ grid values, so those values are not independent physical parameters. The reconstruction problem is to represent the variation across this family with a short latent vector at an acceptable approximation error. The required latent dimension is an empirical result of that comparison; it need not equal N_Θ.

4 Dimensionality reduction with PCA and autoencoders

The response family in Section 3 provides a controlled test of how accurately a short representation can preserve variation across scale and redshift. We compare principal component analysis (PCA) with two nonlinear methods: a convolutional autoencoder and a PCA-assisted autoencoder (PCA-AE). Each method reconstructs the same response surface from $L \in \{2, 4, 6, 8, 10\}$ coordinates. Varying L reveals the balance between representation length and reconstruction accuracy.

4.1 Input representation and normalization

For each sampled parameter combination $\boldsymbol{\Theta}_i$, we form the $N_z \times N_k$ log-amplitude surface

$$Y_i(k, z) = \log_{10} \mathcal{A}_{\boldsymbol{\Theta}_i}(k, z), \qquad X_i(k, z) = \frac{Y_i(k, z) - \overline{Y}(k, z)}{\sigma}. \tag{19}$$

The logarithm reduces the large amplitude range and makes multiplicative differences easier to represent. Here $\overline{Y}$ is the mean training surface, and σ is the root-mean-square deviation from

that mean, averaged over all training surfaces and grid points. Subtracting the mean focuses learning on variations within the family. Dividing by one global scale keeps their relative sizes across the grid unchanged; dividing each grid point by its own standard deviation would change that weighting.

The normalization statistics are fitted using training data and held fixed for validation and final test evaluation. All methods are evaluated after undoing the normalization, $\widehat{Y}_i = \sigma \widehat{X}_i + \overline{Y}$, and, where physical amplitude errors are required, applying $\widehat{\mathcal{A}}_{\boldsymbol{\Theta}_i} = 10^{\widehat{Y}_i}$. The common grid has $N_z = 31$ and $N_k = 101$ as defined in Section 3.6. Writing its shape as $N_z \times N_k$ keeps the distinction between redshift and wavenumber explicit.

4.2 Linear and nonlinear compression

PCA supplies the linear reference. It identifies orthogonal patterns of variation in the training surfaces and orders them by the variance they describe. Flattening X_i into $\boldsymbol{x}_i = \mathrm{vec}(X_i) \in \mathbb{R}^{N_z N_k}$ changes its arrangement without losing information. If $\boldsymbol{v}_a$ is a unit-length principal component, a rank-L reconstruction is

$$c_{ia} = \boldsymbol{v}_a^{\mathsf{T}} \boldsymbol{x}_i, \qquad \widehat{\boldsymbol{x}}_i^{\mathrm{PCA}} = \sum_{a=1}^{L} c_{ia} \boldsymbol{v}_a. \tag{20}$$

The components are fitted only to training data. Because the normalization uses a single global scale, these are the same component directions as for the centred log-surfaces. Retaining fewer components discards some variation, so the accuracy of this approximation must be measured on held-out surfaces.

An autoencoder instead learns an encoder and decoder,

$$\boldsymbol{h}_i = f_\phi(X_i) \in \mathbb{R}^L, \qquad \widehat{X}_i = g_\theta(\boldsymbol{h}_i). \tag{21}$$

The parameters ϕ and θ are adjusted to reduce reconstruction error. Nonlinear transformations allow the same L coordinates to represent relationships that a fixed linear combination may approximate less accurately. The latent vector $\boldsymbol{h}_i$ is the bottleneck: no skip connection carries input information around it. Comparing PCA and autoencoders at equal L tests the accuracy of equally long representations. It does not require a latent coordinate to correspond to one of the N_Θ generating parameters.

4.3 Convolutional autoencoder

The convolutional autoencoder learns directly from X_i. It treats the N_z redshift samples as input channels, each containing a sequence of N_k wavenumbers. A one-dimensional convolution applies the same local filter at successive positions along k and combines information across channels. This design uses the ordered grid to learn patterns spanning neighbouring scales. After the first layer, channels are learned combinations of the input; they no longer represent individual redshifts.

We investigate three-, four-, and five-layer convolutional encoders, with corresponding changes in their dense layers. Figure 13 shows the three-layer architecture reported in Section 5. Three stride-2 convolutions, with kernel lengths 5, 5, and 3, shorten the wavenumber sequences while increasing the number of channels. The final 256×13 feature array is flattened and compressed through dense layers of widths 256, 64, and 16 to L. The decoder uses dense layers and transposed convolutions to restore the original grid dimensions. These operations learn a reconstruction; they are not exact inverses of the encoder. Hidden layers use the smooth nonlinear SiLU activation, while the latent and output layers are linear. The network uses neither dropout nor internal normalization layers.

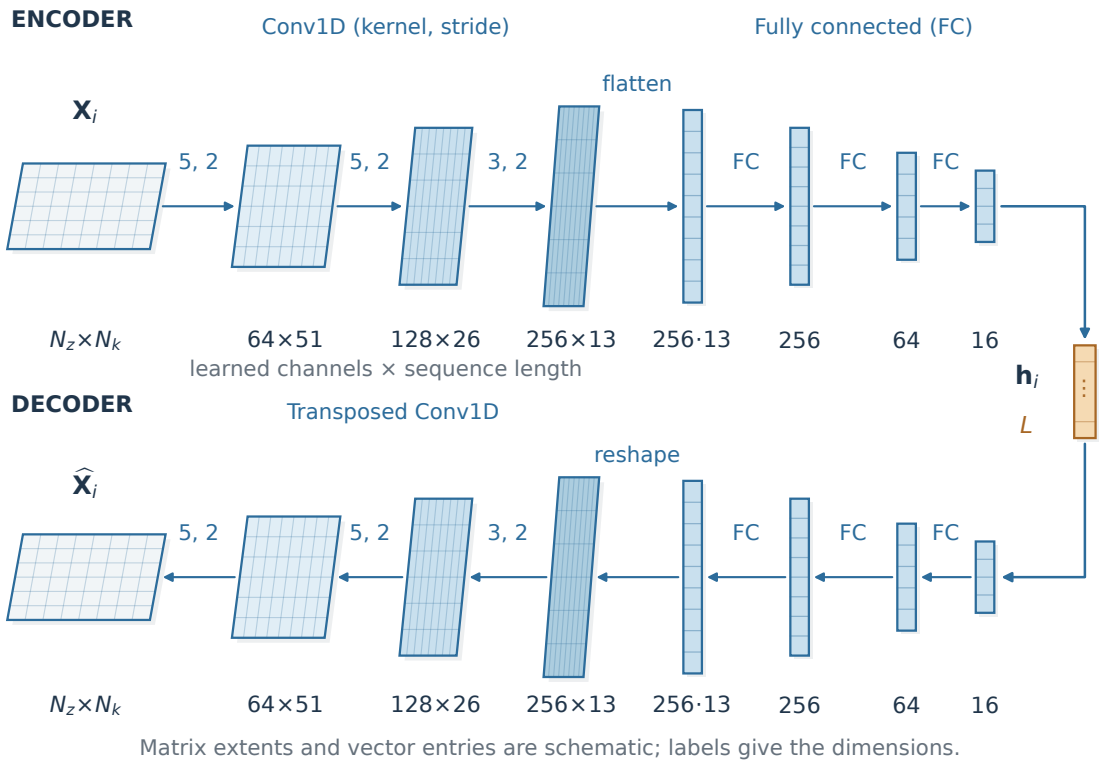


Figure 13: Three-layer convolutional autoencoder. Gridded sheets represent arrays with channel and wavenumber dimensions; strips represent dense vectors, including the L-coordinate bottleneck $\boldsymbol{h}$. Convolution shortens the sequences and mixes channels, and the decoder restores an $N_z \times N_k$ surface. Only the input and output channel axes correspond to redshift. The displayed dimensions specify the implementation; the schematic shapes indicate changes in array size without being drawn to exact scale.

4.4 PCA-assisted autoencoder

PCA-AE tests whether nonlinear compression remains useful after a linear projection has already captured most of the surface variation. It first projects each normalized surface X_i onto a fixed basis of $R = 30$ principal components. Each coefficient is centred and divided by its training standard deviation before entering the neural network. This places coefficients with different natural sizes on comparable input scales. Both the basis and these statistics remain fixed during network training.

The intermediate rank R and final latent width L have different roles. Ordinary PCA in the matched comparison keeps L components; PCA-AE retains R components before learning a nonlinear $R \to L \to R$ map. A linear basis can require more than N_Θ components because the surface depends nonlinearly on its generating parameters. The three-hidden-layer encoder has widths 256, 64, and 16, and the decoder uses the reverse sequence, as shown in Figure 14. Hidden layers use SiLU, and the latent and output layers are linear. The reconstructed coefficients are returned to their original scales and combined with the fixed PCA patterns to recover $\widehat{X}_i$. The inverse normalization in Section 4.1 then restores the log-surface and physical response amplitude.

Rank 30 was chosen to make the initial projection accurate before testing further compression. Among the ranks 25–30 evaluated on the complete validation set, rank 28 was the smallest with a maximum physical relative error below 5%; retaining 30 components reduced that maximum to 4.50%. This threshold is a practical reconstruction criterion, not a precision requirement derived from cosmological observations.

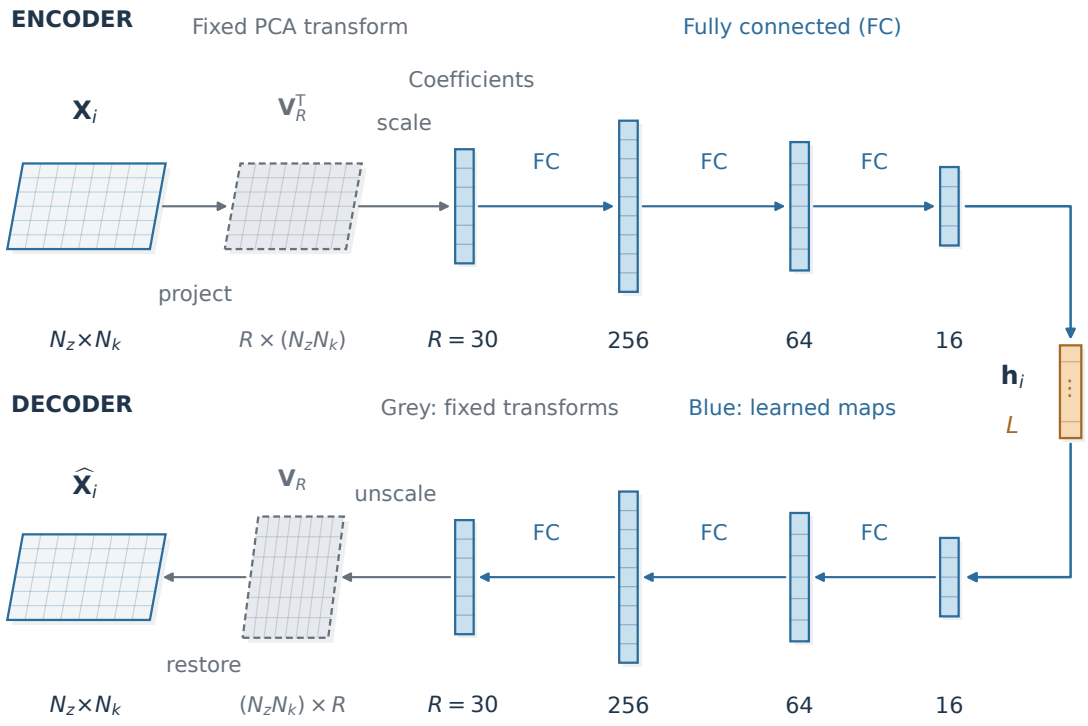


Figure 14: PCA-assisted autoencoder. The $N_z \times N_k$ surface is projected onto a fixed rank-R basis, with $R = 30$, and its coefficients are standardized using training statistics. The neural encoder and decoder compress these coefficients through the same L-coordinate bottleneck used for the convolutional method. Neutral sheets denote surfaces; grey matrices contain the retained patterns $\boldsymbol{V}_R = (\boldsymbol{v}_1, \ldots, \boldsymbol{v}_R)$. Strips denote coefficient or hidden vectors. Scale and unscale denote coefficient standardization and its inverse. The PCA projection, reconstruction, and normalization are fixed; the intervening neural layers are trainable. Schematic sizes indicate representation changes rather than exact dimensional ratios.

The neural network can mix the retained coefficients, but reconstructed variations are restricted to the fixed PCA patterns. Variation in discarded components therefore supplies a reconstruction floor. At $L = 6$, the three-hidden-layer PCA-AE contains 51,076 trainable parameters, compared with 2,041,989 for the three-layer convolutional model. PCA-AE also stores its fixed basis. These methods consequently differ in both representation and model size; an accuracy difference alone cannot isolate the effect of convolution.

4.5 Training and model selection

Training asks the decoder to reproduce its input surface. For a batch of B surfaces, the convolutional network minimizes

$$\mathcal{L}_{\mathrm{MSE}} = \frac{1}{BN_zN_k} \sum_{i=1}^{B} \sum_{j=1}^{N_z} \sum_{\ell=1}^{N_k} \left(\widehat{X}_{ij\ell} - X_{ij\ell} \right)^2 . \tag{22}$$

This objective gives each sampled grid point equal weight in normalized log-amplitude space. PCA-AE uses a weighted coefficient error: the weights account for coefficient standardization and express the retained-component error in the same normalized-surface units. Its full reconstruction error additionally includes the fixed discarded PCA contribution. Validation monitoring includes both contributions.

AdamW updates the network parameters using batches of training surfaces; weight decay discourages unnecessarily large weights. A reduction in the learning rate permits smaller updates when validation improvement slows. Early stopping ends training after sustained lack of improvement, and evaluation uses the saved checkpoint selected by validation error rather than the final training state. Table 2 records the settings and the extended budgets of the reported PCA-AE runs. The different model sizes and training budgets should be considered when comparing their performance.

Table 2: Training settings for the reported convolutional and PCA-assisted autoencoders. Both methods use the shared optimization settings; the epoch budgets include the continued PCA-AE runs.

Setting	Value
Optimization	AdamW; initial learning rate 2×10^{-4}; weight decay 10^{-5}
Batching	training and evaluation batches of 512; final partial batch retained
Numerical controls	gradient-norm limit 1; single-precision training on Apple MPS
Learning-rate schedule	plateau reduction by 0.5; patience 12 epochs; minimum learning rate 10^{-7}
Stopping and checkpoint selection	validation normalized MSE; early-stopping patience 50 epochs; minimum improvement 10^{-7}
Epoch budget	Conv1D: 1,000; three-layer PCA-AE: 1,000, extended to 1,500 for $L = 6$ and $L = 10$; four- and five-layer PCA-AE: 1,500
Randomness	seed 42; deterministic kernels not enforced

We compare latent widths using validation reconstructions, with 99.9% recovered variance as a reference target alongside physical relative-error diagnostics. This target measures compression of the sampled response family; it does not establish adequate accuracy for cosmological inference. The first tested width meeting it need not be the smallest possible width. Each reported neural configuration has one training seed, so its performance has no estimate of variation between independent training runs. The test split is reserved for evaluation after model and training choices have been fixed.

4.6 Reconstruction metrics and interpretation

A small average loss can coexist with a poorly reconstructed surface or a large error in a narrow part of the grid. We therefore measure overall accuracy, physical amplitude errors, and the distribution of errors across surfaces. The definitions in Table 3 apply to any data subset. Section 5 uses the same 10,000 validation surfaces for the reported comparison.

Recovered variance measures improvement over predicting the training mean surface for every input:

$$V_{\mathrm{rec}} = 1 - \frac{\sum_{i,j,\ell} \left(\widehat{Y}_{ij\ell} - Y_{ij\ell} \right)^2}{\sum_{i,j,\ell} \left(Y_{ij\ell} - \overline{Y}_{j\ell} \right)^2}. \tag{23}$$

The sums cover the evaluated surfaces and all $N_z N_k$ grid points. A perfect reconstruction gives $V_{\mathrm{rec}} = 1$; predicting the mean gives zero, and worse predictions can give negative values. Log RMSE measures the residual size in the same log-amplitude space. Both metrics use the same squared residuals, providing two descriptions of the global reconstruction error rather than independent accuracy tests. Neither quantity directly describes the fractional error at a particular scale and redshift.

To assess that error, we return to the physical amplitude. Define

$$e_{ij\ell} = \left| 10^{\widehat{Y}_{ij\ell} - Y_{ij\ell}} - 1 \right|, \qquad r_i = \sqrt{\frac{1}{N_z N_k} \sum_{j=1}^{N_z} \sum_{\ell=1}^{N_k} e_{ij\ell}^2}, \qquad u_i = \max_{j,\ell} e_{ij\ell}. \tag{24}$$

Here $e_{ij\ell}$ is the absolute fractional error at one grid point, r_i is the relative RMSE of one complete surface, and u_i is that surface's largest local error. Percentiles of r_i describe how accuracy varies across the sampled family: at the 95th percentile, approximately 95% of evaluated surfaces have a smaller relative RMSE. This is distinct from a percentile of individual grid-point errors or of each surface's maximum error.

Table 3: Reconstruction metrics and their interpretation. Metrics are defined independently of the data subset used for evaluation.

Metric	Information provided
Recovered variance	Improvement in squared reconstruction error relative to the training mean surface, as in Equation (23).
Log RMSE	Root-mean-square error in $\log_{10} \mathcal{A}_\Theta$, averaged over evaluated surfaces and grid points.
Mean relative error	Mean of $e_{ij\ell}$ over evaluated surfaces and grid points; describes average physical amplitude accuracy.
Maximum relative error	Largest $e_{ij\ell}$ in the evaluated subset; identifies its most severe local reconstruction failure.
Surface relative RMSE, 95th percentile	95th percentile of r_i; summarizes the less accurately reconstructed surfaces.
Surface relative RMSE, 99th percentile	99th percentile of r_i; probes further into the distribution of difficult surfaces.
Surface maximum error, 99th percentile	99th percentile of u_i; describes the upper tail of each surface's worst local error, rather than the largest error in the entire evaluated sample.

Together, these diagnostics distinguish good average reconstruction from reliable performance across the family. They weight the sampled grid directly. Establishing the accuracy needed for a lensing analysis will also require propagating reconstruction errors into its observables and cosmological parameter estimates.

5 Results and discussion

We first compare reconstruction accuracy at equal latent dimension, then examine saved notebook diagnostics from an earlier run of the compact Conv1D architecture (Section 5.3). All scores use the same 10,000 validation surfaces. Each neural configuration contributes one training trajectory, with seed 42; the comparison is not an independent final-test assessment.

5.1 Model comparison and a compact working choice

The comparison includes PCA and three capacity tiers of both Conv1D and PCA-AE at $L \in \{2, 4, 6, 8, 10\}$. The neural models share the training sample and optimization settings of Section 4.5, with the stated differences in model size and epoch budget. The three-layer Conv1D results come from the September run series `20260909-003908` at every width, which replaces the earlier same-seed series throughout. Reported scores are taken from the saved validation artifacts in the project repository; the principal comparisons appear in Table 4. A separate

Conv2D experiment has an incomplete grid and lies outside this comparison; no claim about its relative performance is made here.

Figure 15 shows that both nonlinear methods achieve lower log RMSE and mean relative amplitude error than rank-L PCA at every reported width. For the three-layer Conv1D model, the mean relative error falls from 5.30% at $L = 2$ to 1.21% at $L = 6$ and 0.23% at $L = 10$. At $L = 6$, the reduction relative to PCA is 41.2% in mean relative error and 42.1% in log RMSE. Nonlinear compression therefore preserves this response family more accurately at the same representation length. The comparison concerns approximation quality; it does not imply that neural encoding is faster or uses less shared model storage than PCA.

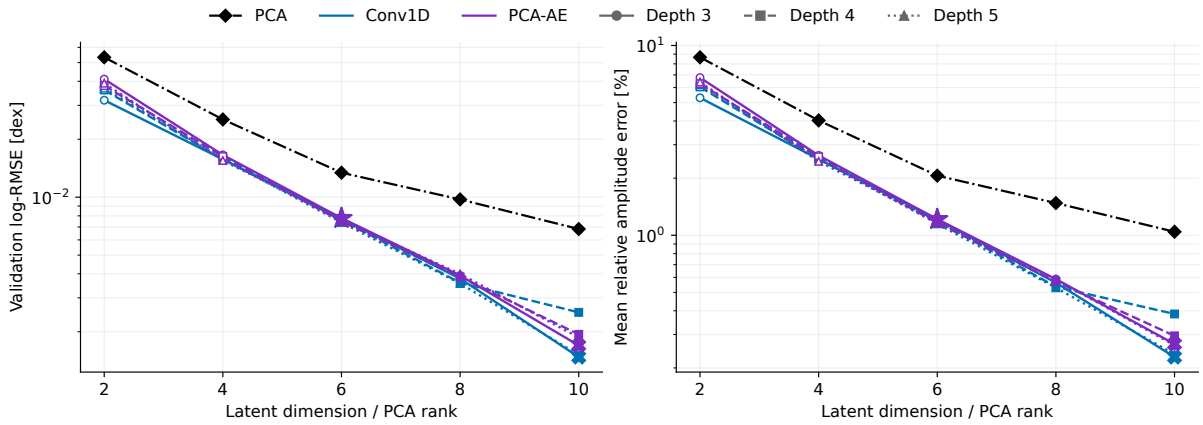


Figure 15: Validation averages at matched latent dimension. Left: RMSE in $\log_{10} \mathcal{A}_\Theta$, in dex. Right: mean absolute relative amplitude error, in percent. Both vertical axes are logarithmic. Blue curves show Conv1D and purple curves show PCA-AE; line styles and marker shapes distinguish the three capacity tiers. Black diamonds show rank-L PCA. Filled neural markers meet the 99.9% recovered-variance reference target; open markers do not. Stars mark the shallowest configuration at the first tested width meeting that target in each neural family. Crosses mark each family's smallest observed log RMSE. All scores use 10,000 validation surfaces and one seed per configuration.

Increasing depth does not yield a consistent improvement. At $L = 6$, for example, the five-layer Conv1D model reduces mean relative error to 1.15%, compared with 1.21% for three layers, but its global maximum error increases from 26.36% to 43.67%. At $L = 10$, the three-layer model has the lowest log RMSE among the reported configurations. Depth here also changes the dense layers, so the comparison tests capacity tiers rather than isolating convolutional depth. Multiple independent seeds would be needed to distinguish systematic architectural effects from training variability.

The tail metrics in Figure 16 also improve on matched-rank PCA, but the ordering among neural configurations depends on the metric and the width. At $L = 6$, the three-layer Conv1D and PCA-AE models have almost identical 95th-percentile surface relative RMS errors (3.14% for both after rounding) and 99th-percentile surface maximum errors (16.64% and 16.79%). Their single largest errors differ more: 26.36% for Conv1D and 48.07% for PCA-AE. A lower percentile does not guarantee a lower absolute maximum; for example, the five-layer Conv1D model at $L = 2$ has a worse global maximum than rank-2 PCA despite better average and percentile errors.

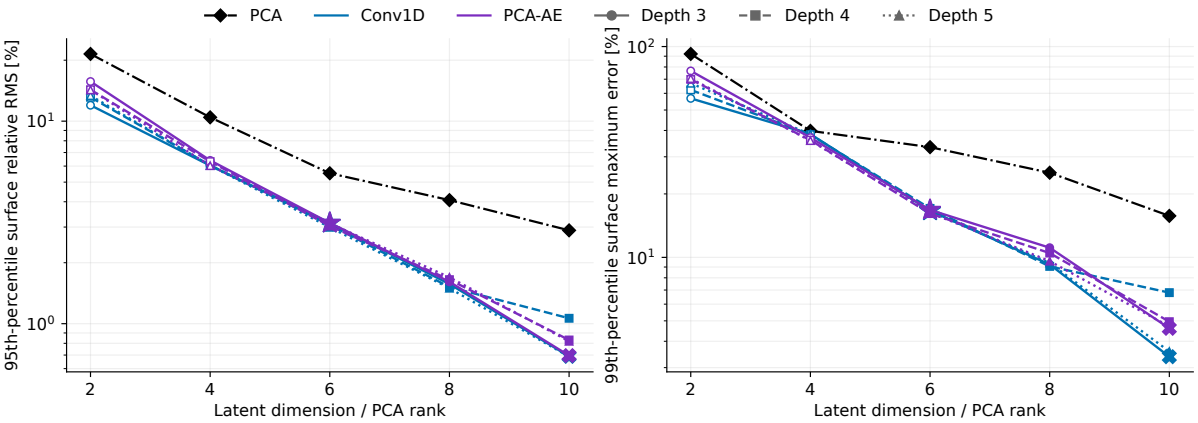


Figure 16: Validation tail errors at matched latent dimension. Left: 95th percentile of the per-surface relative RMS, r_i. Right: 99th percentile of the maximum relative error within each surface. These percentiles are taken over surfaces, not over individual grid points. Both vertical axes are logarithmic. Colours, line styles and markers follow Figure 15.

For detailed diagnostics, we adopt the three-layer Conv1D model at $L = 6$ as a compact working architecture: six is the first tested width to meet the average target, three layers give the smallest Conv1D model at that width, and this run has a smaller observed global maximum than its three-layer PCA-AE counterpart. It recovers 99.92% of the validation variance, with log RMSE 0.00776 dex. Ten-component PCA is somewhat more accurate on average (99.94% recovered variance and 1.04% mean relative error), so six learned coordinates approach, but do not exceed, that linear baseline. The choice is provisional and does not freeze the final-test configuration.

PCA-AE remains a useful alternative. At $L = 6$, its three-layer model has 51,076 trainable parameters, about forty times fewer than Conv1D's 2,041,989, with nearly the same average accuracy. It also stores a fixed rank-30 basis. The preferred method therefore depends on representation length, shared model size, and sensitivity to rare large errors. No measured runtime advantage is claimed. Table 4 summarizes the principal numerical comparisons.

Table 4: Complete-validation results for PCA and the three-layer neural models. Relative errors are percentages; log RMSE is in dex. The percentile definitions follow Figure 16.

Method	L	Log RMSE	Mean	RMS p_{95}	Max p_{99}	Global max
PCA	6	0.01340	2.06	5.53	33.33	55.65
Conv1D	6	0.00776	1.21	3.14	16.64	26.36
PCA-AE	6	0.00779	1.22	3.14	16.79	48.07
PCA	10	0.00683	1.04	2.89	15.73	29.04
Conv1D	10	0.00148	0.23	0.69	3.38	5.17
PCA-AE	10	0.00170	0.27	0.70	4.61	7.67

5.2 PCA and the distribution of surface variation

PCA helps explain why compression is possible. Figure 17 shows how strongly the training surfaces vary along each principal component. The first component accounts for 86.2% of the training variance; two components reach 96.3%, four reach 99.1%, and nine exceed 99.9%. From the seventh component onward, each contributes less than 10^{-3} of the total variance. Most variation is therefore concentrated in a few shared patterns, with progressively smaller

corrections in later components. These fractions describe variance in log-amplitude, not a share of cosmological information.

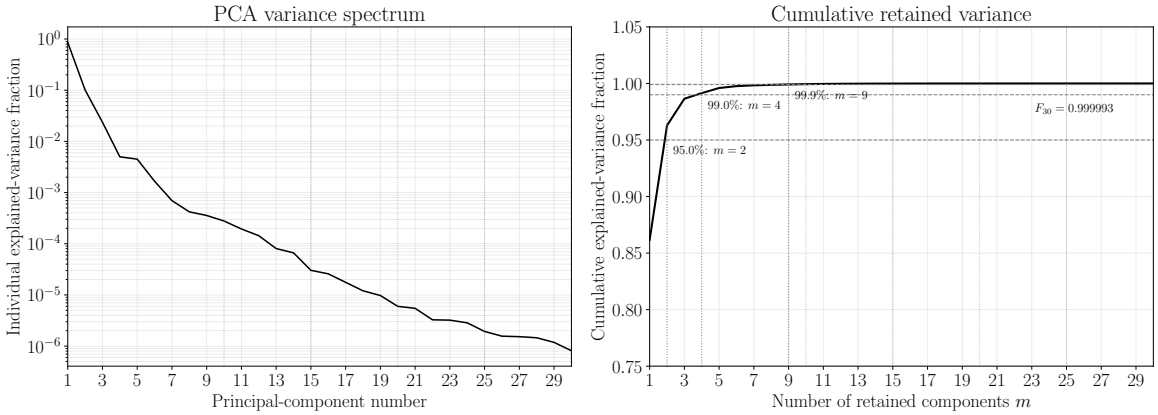


Figure 17: Training PCA spectrum of the stored rank-30 basis. Left: individual explained-variance fractions on a logarithmic axis. Right: cumulative fraction, with the first ranks exceeding 95%, 99% and 99.9% identified. The cumulative fraction at rank 30 is approximately 0.999993. These training fractions differ from recovered variance measured on validation surfaces.

Small-variance components can nevertheless matter for local accuracy. Figure 18 illustrates this on 256 validation surfaces. Evaluations on all 10,000 validation surfaces, performed separately, give rank 10 a mean relative error of 1.04%, yet a maximum of 29.04%. Retaining 30 components reduces the mean to 0.072% and the maximum to 4.50%, with log RMSE 5.38×10^{-4} dex. Among the tested ranks 25–30, rank 28 is the first to fall below the 5% maximum-error reference. The later components therefore make a material difference even though they carry little total variance. Rank-30 PCA is more accurate than the six-coordinate models; its role in PCA-AE is to provide an accurate initial projection before further compression.

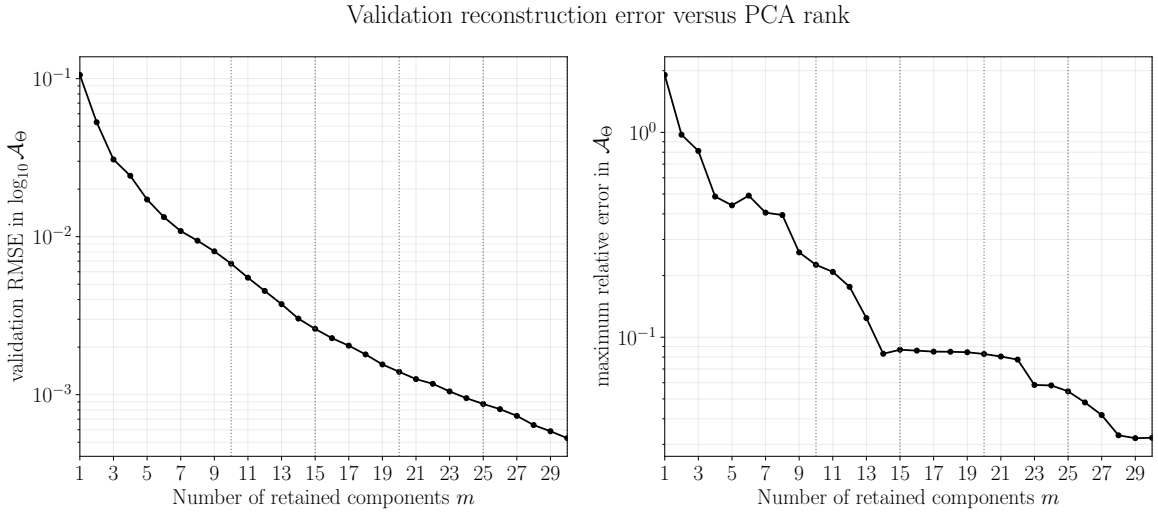


Figure 18: PCA reconstruction errors on 256 validation surfaces at every rank from 1 to 30. Left: RMSE in log-amplitude. Right: maximum relative amplitude error across this subset, expressed as a fraction. Both vertical axes are logarithmic; dotted lines mark reference ranks. The 10,000-surface results in the text are evaluated separately.

5.3 Residual errors of the compact Conv1D model

The original notebook figures in this subsection and the next describe the earlier three-layer, six-coordinate run `20260823-103003`, checkpoint epoch 561. They use the same training and

validation samples and seed 42 as the September comparison, but the learned weights differ. This earlier run recovers 99.92% of the validation variance, with mean relative error 1.25% and maximum error 25.57%. The figures illustrate the error structure and learned coordinates of that earlier fit; its scores are not substituted into Table 4, and the two same-seed runs do not establish variation across independent seeds.

Figure 19 maps the errors of the six-coordinate Conv1D reconstruction. The mean and maximum maps show enhanced errors near the redshift boundaries, particularly at $z = 0$, across part of the scale-transition region, and towards the high-k boundary. The two maps use different colour scales, so brightness cannot be compared directly between them. The lower panels show how often large errors occur. Five percent of validation surfaces have relative RMS above 3.21%; one percent have a maximum local error above 17.17%. These are different summaries of the error distribution and need not identify the same surfaces.

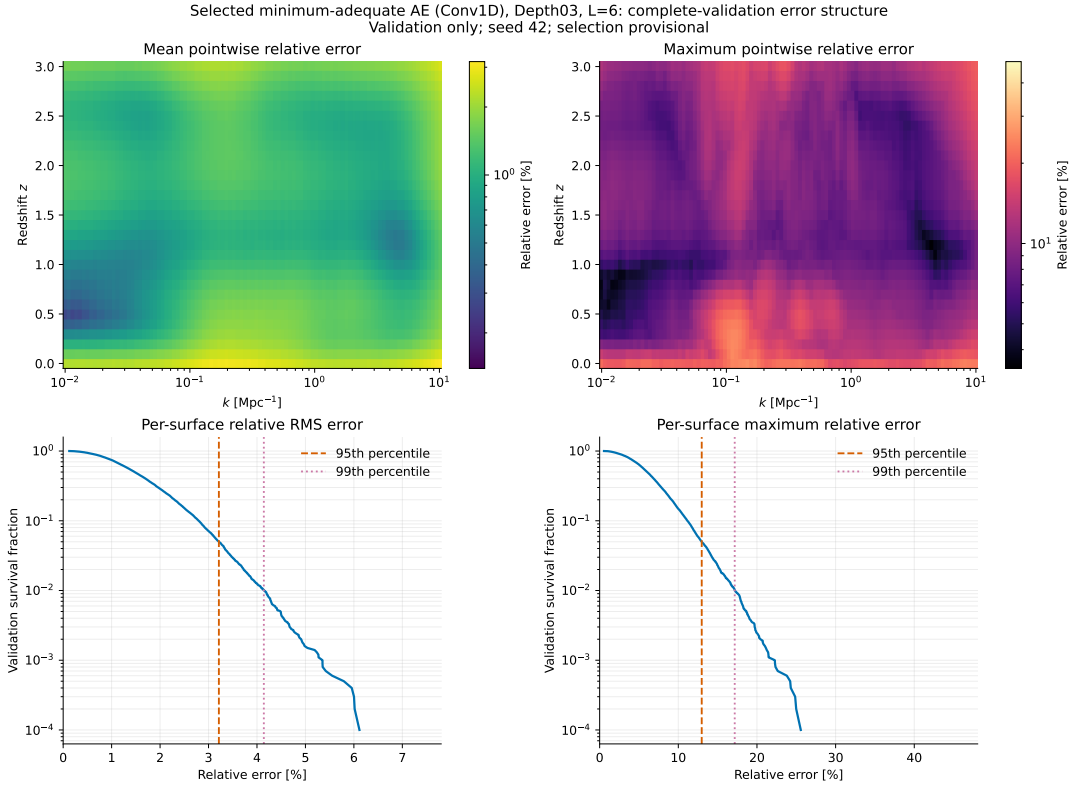


Figure 19: Complete-validation error diagnostics for the three-layer Conv1D model at $L = 6$, run `20260823-103003`, checkpoint epoch 561, using the original notebook export. Top: mean and maximum absolute relative error at each (k, z) location, with separate logarithmic colour scales. Wavenumber is shown on a logarithmic horizontal axis. Bottom: fractions of surfaces with errors at or above each horizontal-axis value, for surface relative RMS and surface maximum error. Dashed and dotted lines mark their respective 95th and 99th percentiles.

These patterns are consistent with the model's freedom to shift the onset and high-k behaviour of $S(k, z)$ and to change its redshift dependence. The maps alone, however, do not show whether the residuals arise mainly from limited representation size, the training objective, sampling, or network architecture. Near the large-scale limit, S approaches unity, but the target surface still varies through $R_z R_L$. It would therefore be incorrect to treat every large-scale grid value as an identical input.

The three worst stored cases in Figure 20 retain the broad structure of the target, but their residuals are spatially concentrated. Their maximum errors are much larger than the population mean. A short representation can therefore be useful for typical surfaces yet remain

inadequate for a demanding local-error requirement. The 99.9% variance target does not resolve that distinction.

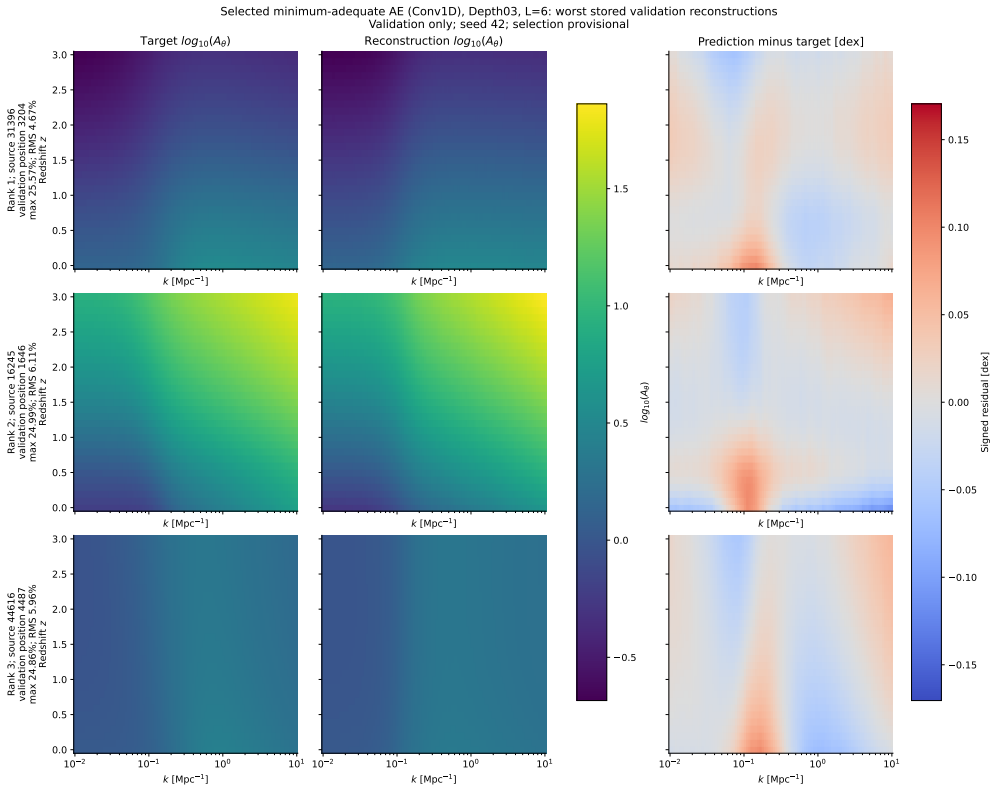


Figure 20: The three validation surfaces with the largest pointwise relative errors for the August Conv1D checkpoint in Figure 19. Rows are ranked by that error. Columns show target log-amplitude, reconstructed log-amplitude, and their signed difference in dex. Target and reconstruction share one colour scale across all rows; residuals use a separate scale symmetric about zero. Axis labels show wavenumber in Mpc^{-1} on a logarithmic scale and redshift. The row labels give maximum relative amplitude errors, which are distinct from the residual colour values.

5.4 Latent geometry and parameter associations

The latent plots provide exploratory diagnostics of the learned representation. Figure 21 shows two projections of the six-dimensional validation sample after each coordinate has been centred and scaled using its training distribution. The colours locate high-error surfaces in these projections, but two views cannot describe the full distribution. The lower-left panel compares medians and central 68% intervals between training and validation; it does not show complete marginal densities. Similar intervals indicate that these summaries are stable. Neither they nor an approximately elliptical projection establish a Gaussian latent distribution.

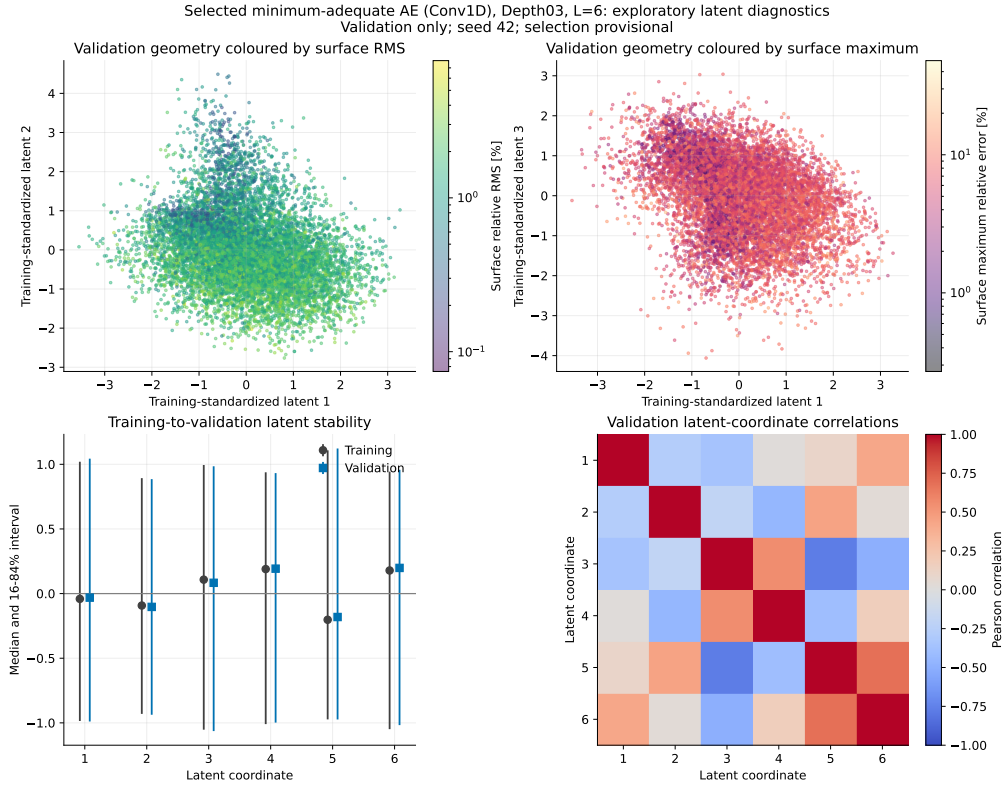


Figure 21: Exploratory latent diagnostics for the August six-coordinate Conv1D checkpoint in Figure 19. Top: validation latent 1 versus latent 2, coloured by surface relative RMS, and latent 1 versus latent 3, coloured by surface maximum error. Lighter colours indicate larger errors, with logarithmic colour scales. Bottom left: coordinate medians and 16th–84th percentile intervals for training and validation, using the same training standardization. Bottom right: Pearson correlations between the six validation coordinates.

Several latent coordinates are correlated with one another. This indicates a linear association between their variations, but it does not measure the number of independent physical directions. The latent axes are also not unique: rotating or otherwise reparameterizing a code can preserve its reconstruction while changing individual correlations. Figure 22 shows associations with the generating parameters. The most visible involve broad redshift evolution and scale-response controls, consistent with their effects in Section 3. A coordinate can combine several parameter influences, and a parameter can affect several coordinates.

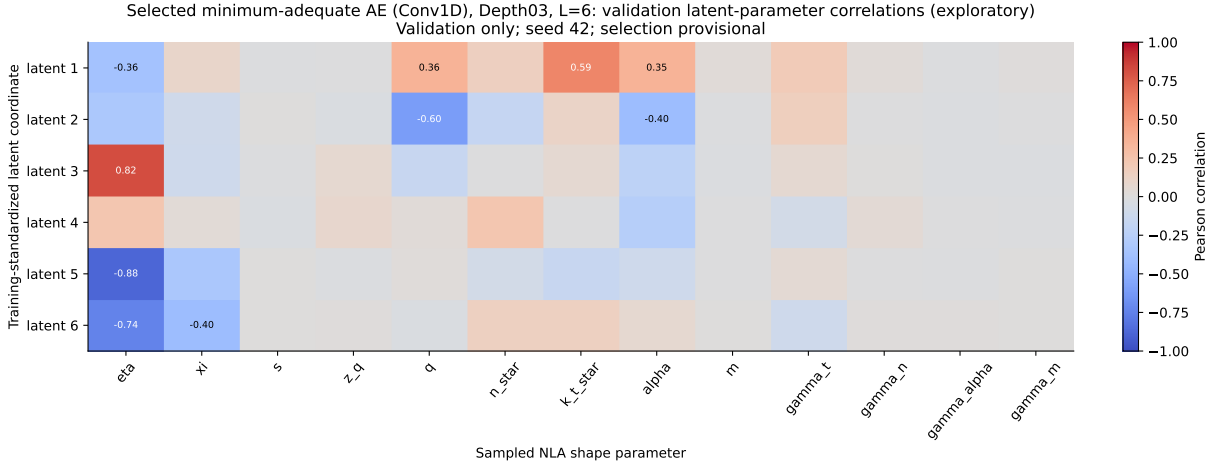


Figure 22: Pearson correlations between the six Conv1D latent coordinates and the 13 shape parameters on the same 10,000 validation surfaces, for the August checkpoint in Figure 19. Red and blue indicate positive and negative correlations. Numerical annotations are shown for $|r| \geq 0.35$ as a readability choice, not a significance threshold. The transition wavenumber uses its sampled physical value $k_{t,*}$, not its logarithm.

A weak Pearson correlation does not imply that a parameter is absent: its influence may be nonlinear or distributed across coordinates. Counting strong entries cannot establish a physical dimension. The choice of six coordinates is justified here by reconstruction accuracy. Parameter-conditioned errors, controlled parameter changes, and nonlinear prediction from the full code would provide stronger tests of which variations are retained.

5.5 Limitations and the next methodological tests

The main limitation is the restricted response family. The functions and sampling ranges are design choices, not constraints from simulations or galaxy observations. The positive shape surface and $q \geq 0$ permit scale-dependent enhancement above the redshift-only baseline but no suppression below it. A fixed-sign response also cannot describe an alignment signal that changes sign across the grid. The tested accuracy therefore applies within this family and its sampling distribution.

Each reported neural configuration uses a single seed. Validation data have guided checkpoint, width, and model choices, so the scores can be optimistic as estimates of final performance. The next priority is to repeat the compact Conv1D and PCA-AE comparisons with independent seeds, including a wider bottleneck as an accuracy reference. Learning curves at several training-set sizes would then test whether more samples improve rare cases. Targeted sampling or weighting may help difficult regions, but any benefit must be measured on a fixed validation distribution so that changes in the population do not masquerade as improved accuracy. A residual architecture (He et al., 2016) is one possible controlled alternative; additional complexity should be justified by a reproducible gain. Final choices should then be frozen before the reserved test set is evaluated.

The present encoder and decoder reconstruct supplied surfaces; they do not provide a calibrated probability distribution from which to draw new ones. A normalizing flow could learn the joint latent distribution through invertible transformations of a simple base density (Papamakarios et al., 2021). Decoded samples would require checks of both surface fidelity and the induced parameter prior. Reducing pairwise correlations would not by itself establish independence or recover physical parameters. A prior learned from the present sampling box would represent that design distribution, not observational knowledge of IA.

Broader applications also require a broader physical target. TATT includes additional contributions to alignment spectra (Blazek et al., 2019), while halo models describe dependencies on central and satellite populations and their properties (Fortuna et al., 2021). Such predictions need not satisfy the single-response relation in Equation (9). Extending this approach may therefore require compressing several signed spectra jointly, with cosmology and galaxy-population information supplied explicitly. That task is more than replacing one positive amplitude in the present model.

6 Summary and conclusion

This work asked whether a 31×101 intrinsic-alignment shape surface can be replaced by a short learned description, and whether that description improves on PCA at the same length. A phenomenological NLA family supplies 100,000 surfaces from 13 sampled shape parameters. PCA is the linear baseline. A one-dimensional convolutional autoencoder and a cheaper PCA-assisted autoencoder are trained at $L \in \{2, 4, 6, 8, 10\}$.

The conclusion is that a nonlinear compressor is useful for this family, and that six Conv1D coordinates are enough for the average target. At equal L, the three-layer Conv1D network improves on PCA: it recovers 98.65% of the validation variance at $L = 2$ against 96.23% for two-component PCA, and 99.92% at $L = 6$, which already approaches ten-component PCA (99.94%). The original notebook diagnostics of the earlier August fit show associations between its latents and the sampled parameters. Their number does not establish the physical dimension; reconstruction accuracy supports the compact choice. At $L = 6$, PCA-AE has comparable averages and percentile errors, while Conv1D has the smaller observed global maximum error.

What the same numbers do not show is a representation that is already safe for cosmology. The ranking is a single-seed validation ranking; the test split has not been read. Mean relative error at $L = 6$ is 1.21%, but the hardest surfaces still reach a 26% local error. The original notebook maps of the August fit locate enhanced residuals at low redshift, around the scale transition, and towards high k. Its latent projections do not establish a Gaussian distribution, and weak pairwise correlations do not show that a physical parameter has been lost. The surfaces themselves come from a hand-specified model, not from a simulation or a survey.

Section 5 already lists the next tests of the compressor, the latent prior, and a more physical alignment family. If a short code of this kind survives those tests, it can enter a weak-lensing analysis as a compact alignment nuisance: fewer free functions to sample, and a clearer separation between alignment uncertainty and the cosmological signal in Stage IV surveys.

Acknowledgements

I thank Thomas Lowery, my school advisor at Oregon Episcopal School, for his guidance while this project was taking shape. His questions and advice helped me keep the work on course, and I am grateful that he made time to talk through difficulties as they arose. I also thank my parents for their patience and support over the months of this study, and my friends for listening, offering encouragement, and reminding me to step back when the writing became slow.

Declaration of AI use

This statement follows the 2026 S.-T. Yau High School Science Award rules on generative AI. Large-language-model tools were used only as an auxiliary aid during manuscript preparation. They did not choose the topic, design the study, invent data or references, or replace the author's scientific argument. Topic selection, research design, core claims, experimental verification, and the academic content of the report remain the author's responsibility.

The main uses were language polishing and grammar correction of prose already drafted by the author, and the drafting of explanatory structure diagrams. The latter include the Section 2 schematics and the Conv1D and PCA-AE architecture drawings in Section 4 (Figures 13 and 14). Other permitted assistance included plotting-code edits and suggestions for report structure. Every formula and numerical result was verified by the author against the project notebooks and saved validation artifacts. AI-assisted wording was not treated as independently written text.

Tools and period: work took place in repeated short sessions during the August–September 2026 writing and revision of the report, not as a single generation of the manuscript. The interface was the Cursor desktop environment together with large-language-model assistants, including GPT-5.6 Sol and Codex for schematic drafts and later Grok for language revision. Exact model versions vary by session and are recorded in the chat logs. Figure 23 shows two representative sessions: grammar and spelling correction, and language polishing of Section 5 with numbers and equations held fixed. The full transcripts will be submitted with the supporting materials ("other materials") for review, as required.

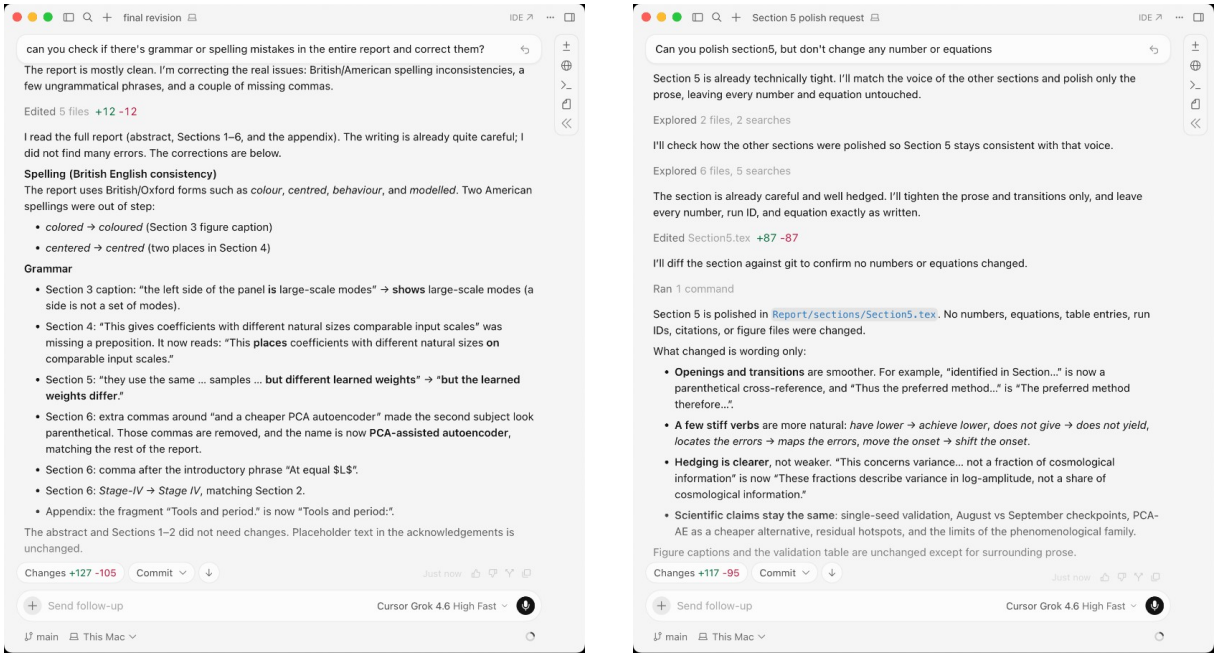


Figure 23: Representative Cursor sessions with Grok 4.6. Left: a request to check grammar and spelling across the report. Right: a request to polish Section 5 without changing numbers or equations. Full chat records are submitted with the supporting materials.

References

Abdul Karim, M., Aguilar, J., Ahlen, S., et al. 2025. DESI DR2 results. II. Measurements of baryon acoustic oscillations and cosmological constraints. *Physical Review D*, 112(8), 083515. doi:10.1103/tr6y-kpc6

Amon, A., Gruen, D., Troxel, M. A., et al. 2022. Dark Energy Survey Year 3 results: Cosmology from cosmic shear and robustness to data calibration. *Physical Review D*, 105(2), 023514. doi:10.1103/PhysRevD.105.023514

Asgari, M., Lin, C.-A., Joachimi, B., et al. 2021. KiDS-1000 cosmology: Cosmic shear constraints and comparison between two point statistics. *Astronomy & Astrophysics*, 645, A104. doi:10.1051/0004-6361/202039070

Bartelmann, M. & Schneider, P. 2001. Weak gravitational lensing. *Physics Reports*, 340(4–5), 291–472. doi:10.1016/S0370-1573(00)00082-X

Blazek, J. A., MacCrann, N., Troxel, M. A., et al. 2019. Beyond linear galaxy alignments. *Physical Review D*, 100(10), 103506. doi:10.1103/PhysRevD.100.103506

Bridle, S. & King, L. 2007. Dark energy constraints from cosmic shear power spectra: impact of intrinsic alignments on photometric redshift requirements. *New Journal of Physics*, 9(12), 444. doi:10.1088/1367-2630/9/12/444

Chisari, N. E., Alonso, D., Krause, E., et al. 2019. Core Cosmology Library: Precision Cosmological Predictions for LSST. *The Astrophysical Journal Supplement Series*, 242(1), 2. doi:10.3847/1538-4365/ab1658

Chisari, N. E. 2025. A rising tide: intrinsic alignments since the turn of the millennium. *The Astronomy and Astrophysics Review*, 33(1), 5. doi:10.1007/s00159-025-00161-8

Choppin de Janvry, J., Dai, B., Gontcho A Gontcho, S., et al. 2025. Cosmic Shear constraints from HSC Year 3 with clustering calibration of the tomographic redshift distributions from DESI. arXiv:2511.18134, version 3 (revised 2026). doi:10.48550/arXiv.2511.18134

Craigie, M., Huff, E., Ting, Y.-S., Ruggeri, R., & Davis, T. M. 2025. Learning Intrinsic Alignments from Local Galaxy Environments. arXiv:2506.05155. doi:10.48550/arXiv.2506.05155

DES Collaboration, Abbott, T. M. C., Aguena, M., et al. 2026. Dark Energy Survey Year 6 Results: Cosmological Constraints from Cosmic Shear. arXiv:2602.10065. doi:10.48550/arXiv.2602.10065

DESI Collaboration, Adame, A. G., Aguilar, J., et al. 2026. DESI DR2 Results IV: Alcock-Paczyński Measurements from the Lyman Alpha Forest and Cosmological Constraints. arXiv:2607.27410. doi:10.48550/arXiv.2607.27410

Eifler, T., Miyatake, H., Krause, E., et al. 2021. Cosmology with the Roman Space Telescope – multiprobe strategies. *Monthly Notices of the Royal Astronomical Society*, 507(2), 1746–1761. doi:10.1093/mnras/stab1762

Euclid Collaboration, Mellier, Y., Abdurro'uf, et al. 2025. Euclid. I. Overview of the Euclid mission. *Astronomy & Astrophysics*, 697, A1. doi:10.1051/0004-6361/202450810

Fortuna, M. C., Hoekstra, H., Joachimi, B., et al. 2021. The halo model as a versatile tool to predict intrinsic alignments. *Monthly Notices of the Royal Astronomical Society*, 501(2), 2983–3002. doi:10.1093/mnras/staa3802

He, K., Zhang, X., Ren, S., & Sun, J. 2016. Deep Residual Learning for Image Recognition. *2016 IEEE Conference on Computer Vision and Pattern Recognition (CVPR)*, 770–778. doi:10.1109/CVPR.2016.90

Hinton, G. E. & Salakhutdinov, R. R. 2006. Reducing the Dimensionality of Data with Neural Networks. *Science*, 313(5786), 504–507. doi:10.1126/science.1127647

Ivezić, Ž., Kahn, S. M., Tyson, J. A., et al. 2019. LSST: From Science Drivers to Reference Design and Anticipated Data Products. *The Astrophysical Journal*, 873(2), 111. doi:10.3847/1538-4357/ab042c

Jolliffe, I. T. & Cadima, J. 2016. Principal component analysis: a review and recent developments. *Philosophical Transactions of the Royal Society A: Mathematical, Physical and Engineering Sciences*, 374(2065), 20150202. doi:10.1098/rsta.2015.0202

Li, S.-S., Hoekstra, H., Kuijken, K., et al. 2023a. KiDS-1000: Cosmology with improved cosmic shear measurements. *Astronomy & Astrophysics*, 679, A133. doi:10.1051/0004-6361/202347236

Li, X., Zhang, T., Sugiyama, S., et al. 2023b. Hyper Suprime-Cam Year 3 results: Cosmology from cosmic shear two-point correlation functions. *Physical Review D*, 108(12), 123518. doi:10.1103/PhysRevD.108.123518

Pandya, S., Yang, Y., Van Alfen, N., Blazek, J., & Walters, R. 2025. IAEmu: Learning Galaxy Intrinsic Alignment Correlations. *The Open Journal of Astrophysics*, 8. doi:10.33232/001c.151749

Papamakarios, G., Nalisnick, E., Rezende, D. J., Mohamed, S., & Lakshminarayanan, B. 2021. Normalizing Flows for Probabilistic Modeling and Inference. *Journal of Machine Learning Research*, 22(57), 1–64. https://jmlr.org/papers/v22/19-1028.html

Planck Collaboration, Aghanim, N., Akrami, Y., et al. 2020a. Planck 2018 results. I. Overview and the cosmological legacy of Planck. *Astronomy & Astrophysics*, 641, A1. doi:10.1051/0004-6361/201833880

Planck Collaboration, Aghanim, N., Akrami, Y., et al. 2020b. Planck 2018 results. VI. Cosmological parameters. *Astronomy & Astrophysics*, 641, A6. doi:10.1051/0004-6361/201833910

Riess, A. G., Filippenko, A. V., Challis, P., et al. 1998. Observational Evidence from Supernovae for an Accelerating Universe and a Cosmological Constant. *The Astronomical Journal*, 116(3), 1009–1038. doi:10.1086/300499

Spurio Mancini, A., Piras, D., Alsing, J., et al. 2022. CosmoPower: emulating cosmological power spectra for accelerated Bayesian inference from next-generation surveys. *Monthly Notices of the Royal Astronomical Society*, 511(2), 1771–1788. doi:10.1093/mnras/stac064

Wright, A. H., Stölzner, B., Asgari, M., et al. 2025. KiDS-Legacy: Cosmological constraints from cosmic shear with the complete Kilo-Degree Survey. *Astronomy & Astrophysics*, 703, A158. doi:10.1051/0004-6361/202554908